

Calibration Concordance for Astronomical Instruments via Multiplicative Shrinkage

Yang Chen,^{*} Xiao-Li Meng,[†] Xufei Wang,[‡] David A. van Dyk,[§]
Herman L. Marshall,[¶] Vinay L. Kashyap^{||}

June 18, 2022

Abstract

Calibration data are often obtained by observing several well-understood objects simultaneously with multiple instruments, such as satellites for measuring astronomical sources. Analyzing such data and obtaining proper concordance among the instruments is challenging when the physical source models are not well understood, when there are uncertainties in “known” physical quantities, or when data quality varies in ways that cannot be fully quantified. Furthermore, the number of model parameters increases with both the number of instruments and the number of sources. Thus, concordance of the instruments requires careful modeling of the mean signals, the intrinsic source differences, and measurement errors. In this paper, we propose a log-Normal hierarchical model and a more general log-t model that respect the multiplicative nature of the mean signals via a half-variance adjustment, yet permit imperfections in the mean modeling to be absorbed by residual variances. We present analytical solutions in the form of power shrinkage in special cases and develop reliable Markov chain Monte Carlo (MCMC) algorithms for general cases, both of which are available in the `Python` module *CalConcordance*. We apply our method to several data sets including a combination of observations of *active galactic nuclei* (AGN) and spectral line emission from the *supernova remnant* E0102, obtained with a variety of X-ray telescopes such as *Chandra*, *XMM-Newton*, *Suzaku*, and *Swift*. The data are compiled by the *International Astronomical Consortium for High Energy Calibration* (IACHEC). We demonstrate that our method provides helpful and practical guidance for astrophysicists when adjusting for disagreements among instruments.

Keywords: Adjusting attributes; shrinkage estimator; Bayesian hierarchical model; log-Normal model; half-variance adjustment; log-t model.

^{*}Yang Chen is Assistant Professor, Department of Statistics and Michigan Institute for Data Science (MIDAS), University of Michigan, Ann Arbor, MI 48109; email: ychenang@umich.edu.

[†]Xiao-Li Meng is Whipple V. N. Jones Professor of Statistics, Harvard University, Cambridge, MA 02138.

[‡]Xufei Wang was a Ph.D. candidate, Department of Statistics, Harvard University, Cambridge, MA 02138.

[§]David A. van Dyk is a Professor of Statistics and Head of the Department of Mathematics at Imperial College London, London, UK SW7 2AZ.

[¶]Herman Marshall is Astrophysicist, MIT Kavli Institute, Cambridge, MA 02139.

^{||}Vinay Kashyap is Astrophysicist, Harvard-Smithsonian Center for Astrophysics, Cambridge, MA 02138.

1 Introducing Calibration Concordance

The calibration of instruments is fundamental for comparing or combining measurements obtained with different instruments. Typically, calibration is conducted by using each of several instruments to measure one or more well-understood objects, e.g., astronomical sources. The resulting data are used to develop adjustments that can be applied to future observations to obtain reliable absolute measurements. Convenient adjustments, such as ad hoc affine or ratio adjustments, however, often result in poor calibration, and without justifiable quantification of the calibration error that is essential for assessing the uncertainty of the final estimates of interest. The main difficulty of deriving reliable adjustments for instruments springs from the variations that are intrinsic to the sources and to the instruments, in addition to individual measurement errors.

First, the physical models, derived using various approximations based on scientists’ current understandings of the instruments, may not be as reliable as we hope. Second, “known” physical quantities are typically estimates themselves; even when their estimated errors are available, standard plug-in estimators and error propagation techniques may lead to biased and often overly optimistic results. Third, data quality varies in ways that cannot be fully quantified, especially across instruments or in the presence of outliers. Last, the number of unknown model parameters increases with the number of instruments and the number of sources, leading to well-known model challenges. Together these challenges and subtleties expose that, although calibration problems have a long history, principled statistical adjustments are not in routine use or even understood.

In this paper, we attempt to fill this gap for a variety of astronomical instruments, by developing hierarchical models that respect the physical models for the mean signals, while permitting the modeling imperfections to be captured by residual variances. We build reasonably effective fitting algorithms via Hamiltonian Monte Carlo, and the corresponding software, *CalConcordance*, which is then used to test our models on simulated data. We then apply our methods to several datasets from the *International Astronomical Consortium for High Energy Calibration* (IACHEC).

1.1 Calibration Concordance for Astronomical Instruments

In astrophysics, various instruments such as telescopes are used by different teams of scientists to understand intrinsic properties of astronomical objects, i.e., sources such as stars. Although it

is possible to make relative comparisons of different sources observed with the same instrument, unless the instruments are properly calibrated (Sembay et al., 2010), we cannot make reliable absolute measurements or make comparisons of sources observed with different instruments. Therefore, calibration of different instruments is an important, and on-going, problem for astrophysicists (Seward, 1992; Matthews and Havey, 2010; Nevalainen et al., 2010; Tsujimoto et al., 2011; Read et al., 2014; Schellenberger et al., 2015; Madsen et al., 2016).

As an example, space-based (e.g., X-ray) telescope calibration (Schwartz, 2014) is handled in two phases: first, under controlled laboratory conditions (“ground” calibration), and second, while in space using astrophysical sources (“in-flight” calibration; see Guainazzi et al. (2015, see)). At each phase, the same set of well-understood sources is observed with multiple instruments. The intent of in-flight calibration is usually to verify ground calibration but imperfect laboratory conditions and evolving instrument characteristics (while in-flight) may result in discrepancies between different telescopes. The task of developing reliable adjustments for astronomical instruments based on observing multiple sources with multiple instruments is known as the *calibration concordance problem*, which aims to develop a *concordance* in the calibration among these astronomical instruments. This paper is motivated by the need for a statistically principled solution and it is a joint effort between astrophysicists and statisticians, both of whose expertise are needed in order to appropriately quantify the uncertainties while incorporating scientific understanding and experts’ knowledge and judgments.

For the calibration problem discussed in this paper, the following two concepts are essential.

- **Flux of an astronomical source.** The absolute flux is the quantity of luminous energy incident upon the aperture of a telescope per unit area per unit time. The absolute flux of an astronomical source depends on the luminosity of the object and its distance from the Earth, both of which are intrinsic to the object. For a fixed source spectrum, i.e., the distribution of photon energies, the *measured flux* is proportional to the number of photons *detected* by an astronomical instrument. If the spectrum changes, or the detector on the instrument changes, then so will the number of photons and the measured flux.
- **Effective Area for an instrument.** The geometric area of a telescope (instrument) is an upper bound on its capacity to collect photons. Many factors can reduce the efficiency of

photon collection, including mirror reflectivity, structural obscuration, filter transmission, detector sensitivity, etc. This reduction in efficiency is also photon-energy dependent. The *Effective Area* is the equivalent geometric size of an ideal detector that would have the same collection capability and it is empirically measured or theoretically calculated and tabulated as a function of energy. The instrument’s Effective Area is used to estimate the absolute flux of an astronomical source given its measured flux. Since the Effective Area varies with energy, astronomers often consider different energy bands for comparing observations as different instruments, a convention we adopt (George et al., 1992; Graessle et al., 2006).

The calibration problem arises because the Effective Areas of the instruments are not known precisely (Drake et al., 2006; Kashyap et al., 2008; Lee et al., 2011; Xu et al., 2014), and hence different instruments can yield substantially different measured fluxes for the same unvarying source. Therefore, the problem of calibration among different instruments is equivalent to reliably estimating the Effective Area of each instrument. By *reliably* we mean that, after proper adjustments of the Effective Areas, instruments measuring a common source should agree within *stated and scientifically acceptable* statistical uncertainty on the absolute flux of each source.

1.2 A Multiplicative Physical Model

Suppose we observe photon counts, $\{c_{ij}\}$, where i indexes N instruments and j indexes M objects/sources. The observed photon count c_{ij} is known to follow a Poisson model with intensity C_{ij} , which is affected by the Effective Area A_i and flux F_j in the following way. Because source fluxes have units of photons per second and per square centimeter, they are multiplied by instrument Effective Areas and a known factor T_{ij} to obtain expected photon counts:

$$C_{ij} = T_{ij}A_iF_j, \quad 1 \leq i \leq N, \quad 1 \leq j \leq M. \quad (1.1)$$

Here the multiplicative constant T_{ij} contains the exposure time, as well as other factors that can be calculated approximately by astrophysicists; see Marshall et al. (2017) for details. Fundamentally, (1.1) implies that the Effective Area for a particular instrument remains the same regardless of which source *in the chosen group* it is applied to (and vice versa). Clearly then, by using a more homogeneous subgroup of sources, we can increase the chance that (1.1) holds, as we illustrate in

Section 4.1. Of course, there is no free lunch – by using a subgroup, we have less data and hence higher variability of our estimator, a bias-variance trade-off. With this in mind, we can regard T_{ij} as a fixed known constant, and any real uncertainties related to T_{ij} can be partially captured by our residual modeling discussed later, and more fully in subsequent work.

Prior to observing $\{c_{ij}\}$, astronomers have initial estimates a_i for A_i , obtained from ground-based or dedicated in-flight calibration measurements. Comparing with estimated fluxes of well-understood sources, astronomers can also place a reasonable prior bound on the margin of relative error in a_i at about 20%. Additional prior knowledge on the measurement errors in $\{c_{ij}\}$ is also available. How to utilize such prior information, and whether these estimated uncertainties suffice to explain the variations in the data, are among the questions that we investigate in this paper.

For the rest of this paper, Section 2 describes a statistical model for calibration concordance, a log-Normal hierarchical model, and extends it to a more general log-t model to handle outliers. Using simulated and real data, Section 3 and Section 4 assess and verify the empirical performance of our methods. Section 5 briefly discusses a likelihood approach and its connection to our Bayesian approach, and future work. All numerical results are reproducible using the *Python* code and data available on GitHub at <https://github.com/astrostat/Concordance>.

2 Building and Fitting the Proposed Concordance Models

2.1 Modeling Multiplicative Means

To make the distinctions between observed quantities (e.g., estimator) and unknown quantities (e.g., estimand) crystal clear, we adopt the convention that the former is denoted by lowercase (English) letters and the latter uppercase, whenever feasible. We express (1.1) as

$$\log C_{ij} - \log T_{ij} = \log A_i + \log F_j = B_i + G_j \quad (2.1)$$

where $B_i = \log A_i$ and $G_j = \log F_j$. While this is a trivial relationship among the *estimands*, it does not hold for their corresponding *estimators*. In fact, if we let $y_{ij} = \log c_{ij} - \log T_{ij}$ (and ignore the issue of $c_{ij} = 0$ for now), $b_i = \log a_i$ and $g_j = \log f_j$, we cannot expect even that $y_{ij} = b_i + g_j + \epsilon_{ij}$ and that ϵ_{ij} is independent of $\{b_i, g_j\}$ with mean zero. If both were true, it

would imply (incorrectly) that the expectation of y_{ij} is determined by b_i and g_j , rather than by their respective estimands: B_i and G_j .

Instead, we can assume that the measurement error in c_{ij} for C_{ij} is multiplicative (i.e., in terms of a percentage) and postulate the regression model

$$y_{ij} = \alpha_{ij} + B_i + G_j + e_{ij}, \quad e_{ij} \stackrel{\text{indep}}{\sim} \mathcal{N}(0, \sigma_i^2). \quad (2.2)$$

Thus the observed counts $\{c_{ij}\}$ are modeled as log-Normal variables, which is an approximation that works well when $\{c_{ij}\}$ (and hence $\{C_{ij}\}$) are reasonably large, as in our applications. Nevertheless, when $c_{ij} = 0$ occurs (as in our simulation study), we use the conventional replacement 0.5 for 0. This leads to a zero-modified Poisson, \tilde{c} , of an original Poisson, c , with mean λ , and

$$\mathbb{E}(\tilde{c}) = \lambda + 0.5e^{-\lambda}, \quad \text{Var}(\tilde{c}) = \lambda(1 - e^{-\lambda}) + 0.25e^{-\lambda}(1 - e^{-\lambda}). \quad (2.3)$$

With reasonably large λ , \tilde{c} approximates c extremely well, an approximation we use below.

We set $\alpha_{ij} = -0.5\sigma_i^2$ as the half-variance correction for the multiplicative mean modeling in (1.1) to ensure that $\mathbb{E}(c_{ij}) = C_{ij}$. Ignoring the difference between c_{ij} and \tilde{c}_{ij} , this can be verified via the moment generating function of the Normal distribution, which yields

$$\mathbb{E}(c_{ij}) = T_{ij}\mathbb{E}(e^{y_{ij}}) = T_{ij}e^{\alpha_{ij}+0.5\sigma_i^2}e^{B_i}e^{G_j} = T_{ij}A_iF_j = C_{ij}.$$

For convenience, when (and *only when*) σ_i^2 is known, we treat $y'_{ij} = y_{ij} - \alpha_{ij} = y_{ij} + 0.5\sigma_i^2$ as data.

Since $b_i = \log a_i$ is astrophysicists' initial estimate of B_i with uncertainty determined by their knowledge of instrument i , we can view it as a *noisy observation* with known variance τ_i^2 :

$$b_i \stackrel{\text{indep}}{\sim} \mathcal{N}(B_i, \tau_i^2). \quad (2.4)$$

Together with (2.2), this gives a multivariate Normal regression model. One can then apply the maximum likelihood approach, as discussed in Section 5.1. We, however, adopt a Bayesian perspective, by formulating the experts' knowledge as a prior distribution for B_i :

$$B_i \stackrel{\text{indep}}{\sim} \mathcal{N}(b_i, \tau_i^2). \quad (2.5)$$

This reversal can be justified more formally by viewing it as the posterior distribution derived from (2.4) with a flat prior distribution on B_i . We take a Bayesian approach primarily because 1) characterizing empirical knowledge via a prior distribution is an accepted practice in the astronomical

community, as it is the process of updating prior knowledge using data to provide updated estimators along with their uncertainties; 2) the maximum-a-posteriori (MAP) estimators obtained from the hierarchical model are *shrinkage estimators*, which intuitively summarize how experts’ prior knowledge and information from various instruments and sources are best combined; and 3) since the dimension of the parameter space is large and the parameters of interest are highly correlated, Bayesian computational methods, such as MCMC algorithms, are better suited for exploring the parameter space than optimization algorithms.

Any model involves approximations and simplifications. Our log-Normal model is an approximation, and may work poorly when the counts are small. Nevertheless, we adopt the log-Normal model because both its mean and variance are free parameters, providing flexibility for the variance term to (partially) capture imperfections in the mean model, especially the unspecified approximation or estimation error in the correcting factor T_{ij} ; see Section 3.1 for a discussion in our numerical experiments. As a matter of the fact, the data we received were the original observed photon counts divided by T_{ij} , and hence they are no longer (Poisson) counts.

Second, in (2.2), the variance for the measurement error is assumed to depend only on the instrument. This assumption works reasonably well in our applied examples, but generally, each e_{ij} can have its own variance, σ_{ij}^2 , i.e., $e_{ij} \stackrel{\text{indep}}{\sim} \mathcal{N}(0, \sigma_{ij}^2)$. When $\{\sigma_{ij}^2\}$ are unknown, we need to constrain them to ensure identifiability. Other possible constraints include forcing the variances to be only source-dependent or to be additive, i.e., $\sigma_{ij}^2 = \omega_i^2 + \lambda_j^2$. We start with the *known variance model* because astronomers provided their “guesstimates”, that is, their best guesses, of σ_{ij}^2 . However, as illustrated in subsequent sections, the *unknown variance model*, which is our primary model, is more flexible, robust, and hence recommended in practice. This is because the inferred adjustment of Effective Areas could be either overly-optimistic or overly-conservative if the specified $\{\sigma_{ij}^2\}$ are inaccurate. Unfortunately, this is often the case in practice owing to an incomplete understanding of the uncertainties in measurements or in data preprocessing.

Finally, because not all sources can be observed with all instruments, we let J_i be the set of indexes of the objects observed by detector i and I_j the set of indexes of the instruments that observe object j . If the set of objects observed with each instrument reflect a biased selective mechanism, our model might produce misleading results. However, this is not a deep concern for

us for several reasons. First, the instruments we consider share a broad common energy passband. Second, the likelihood of a source not being observed because it is too faint is low. Furthermore, the vagaries of scheduling introduces large variations in the completeness achievable in a fleet of spacecraft — each has several independent intrinsic constraints that are related to the shape of their orbits; their Sun, Moon, and Earth avoidance angles; and even their thermal environment histories; making scheduling of simultaneous observations difficult — renders this selection bias negligible. Consequently, astronomers feel comfortable about our model assumption that the missing-data mechanism is ignorable (Rubin, 1978).

2.2 Log-Normal Hierarchical Model and Its Posterior Sampling

To embed our log-Normal model (2.2) into a Bayesian hierarchical model, we also need a prior for G_j , which is the usual flat prior since astronomers do not feel comfortable assuming anything else. When $\{\sigma_i^2\}$ are treated as unknowns, we adopt independent Inverse-Gamma distributions with shape parameter α and scale parameter β , the value of which are chosen to reflect the astronomers' prior knowledge. That is, we assume

$$\begin{aligned} y_{ij} \mid \mathbf{B}, \mathbf{G}, \boldsymbol{\sigma}^2 &\stackrel{\text{indep}}{\sim} \mathcal{N}\left(-\frac{\sigma_i^2}{2} + B_i + G_j, \sigma_i^2\right), \\ \sigma_i^2 &\stackrel{\text{indep}}{\sim} \text{Inv-Gamma}(\alpha, \beta), \quad B_i \stackrel{\text{indep}}{\sim} N(b_i, \tau_i^2), \quad G_j \stackrel{\text{indep}}{\sim} \text{flat prior} \end{aligned} \quad (2.6)$$

where $\mathbf{B} = (B_1, \dots, B_N)^\top$, $\mathbf{G} = (G_1, \dots, G_M)^\top$, $\boldsymbol{\sigma}^2 = (\sigma_1^2, \dots, \sigma_N^2)^\top$, and $\boldsymbol{\tau}^2 = (\tau_1^2, \dots, \tau_N^2)^\top$, and \top denotes the usual transpose. Under (2.6), we can show that (see Appendix B.1) the posterior distribution is proper with the weakest condition possible: each source is observed by at least one instrument. This theoretical guarantee is especially important because the number of parameters, $2N + M$, varies with the number of observations, NM . Furthermore, the MAP estimator of each σ_i^2 is bounded away from zero by a constant which depends only on the hyperparameters and the total number of sources (Section 2.3). Last, the use of proper conjugate priors for σ_i^2 avoids the problem of unbounded posterior distribution, which can occur when we use constant prior distributions for $\{\sigma_i^2\}$. We also remark here that, because σ_i^2 enters both the variance and mean in (2.6), the prior impact on the posterior inference is much more nuanced, as we discuss in the context of astrophysical applications (Section 4.1).

Under (2.6), the posterior density of $\{\mathbf{B}, \mathbf{G}, \boldsymbol{\sigma}^2\}$, if it exists, is proportional to

$$\left[\prod_{i=1}^N \sigma_i^{-|J_i|-2-2\alpha} \right] \exp \left\{ -\frac{1}{2} \sum_{i=1}^N \sum_{j \in J_i} \frac{(y_{ij} + 0.5\sigma_i^2 - B_i - G_j)^2}{\sigma_i^2} - \sum_{i=1}^N \left[\frac{(b_i - B_i)^2}{2\tau_i^2} + \frac{\beta}{\sigma_i^2} \right] \right\}. \quad (2.7)$$

Conditioning on $\boldsymbol{\sigma}^2$, this is an $(N + M)$ -dimensional Gaussian density for the column vector $\boldsymbol{\theta} \equiv (\mathbf{B}, \mathbf{G})$. A simple way of deriving its mean $\boldsymbol{\mu}(\boldsymbol{\sigma}^2)$ and covariance $\boldsymbol{\Sigma}(\boldsymbol{\sigma}^2)$ is to use partial derivatives of $L(\boldsymbol{\theta}, \boldsymbol{\sigma}^2)$, the log of the posterior density given in (2.7). Let

$$\boldsymbol{\gamma}(\boldsymbol{\sigma}^2) = \frac{\partial L(\boldsymbol{\theta}, \boldsymbol{\sigma}^2)}{\partial \boldsymbol{\theta}} \Big|_{\boldsymbol{\theta}=0} \quad \text{and} \quad \boldsymbol{\Omega}(\boldsymbol{\sigma}^2) = -\frac{\partial^2 L(\boldsymbol{\theta}, \boldsymbol{\sigma}^2)}{\partial \boldsymbol{\theta}^2}. \quad (2.8)$$

By the form of the Gaussian density, $\boldsymbol{\mu}(\boldsymbol{\sigma}^2) = \boldsymbol{\Omega}^{-1}(\boldsymbol{\sigma}^2) \boldsymbol{\gamma}(\boldsymbol{\sigma}^2)$ and $\boldsymbol{\Sigma}(\boldsymbol{\sigma}^2) = \boldsymbol{\Omega}^{-1}(\boldsymbol{\sigma}^2)$. Evaluating these derivatives yields $\boldsymbol{\gamma} = (\gamma_1, \dots, \gamma_N, \gamma_{N+1}, \dots, \gamma_{N+M})^\top$ and $\boldsymbol{\Omega}$ as functions of $\boldsymbol{\sigma}^2$:

$$\gamma_i = \frac{\sum_{j \in J_i} y_{ij}}{\sigma_i^2} + \frac{b_i}{\tau_i^2} + 0.5|J_i|, \quad i = 1, \dots, N, \quad \gamma_{j+N} = \sum_{i \in I_j} \frac{y_{ij}}{\sigma_i^2} + 0.5|I_j|, \quad j = 1, \dots, M, \quad (2.9)$$

$$\boldsymbol{\Omega}(\boldsymbol{\sigma}^2) = \begin{pmatrix} \mathbf{D}_N & \mathbf{D}\mathbf{R} \\ \mathbf{R}^\top \mathbf{D} & \mathbf{D}_M \end{pmatrix}, \quad \text{where} \quad \begin{aligned} \mathbf{D}_N &= \text{Diag}\{|J_i|\sigma_i^{-2} + \tau_i^{-2}, \quad i = 1, \dots, N\}, \\ \mathbf{D}_M &= \text{Diag}\{\sum_{i \in I_j} \sigma_i^{-2}, \quad j = 1, \dots, M\}, \end{aligned} \quad (2.10)$$

$\mathbf{D} = \text{Diag}\{\sigma_i^{-2}, \quad i = 1, \dots, N\}$, and $\mathbf{R} = \{r_{ij}\}$, with \mathbf{R} the $N \times M$ data “recoding matrix”, that is, $r_{ij} = 1$ if instrument i is used for source j , and $r_{ij} = 0$ otherwise. If all the instruments measure all the sources (as in our applications), \mathbf{R} and $\mathbf{D}\mathbf{R}$ are rank-one. In this case, the inverse of $\boldsymbol{\Omega}(\boldsymbol{\sigma}^2)$, which is the variance-covariance matrix of (\mathbf{B}, \mathbf{G}) given $\boldsymbol{\sigma}^2$, can be calculated analytically using properties of block matrix and the Woodbury matrix identity (Woodbury, 1950); see Appendix C.

When $\boldsymbol{\sigma}^2$ is unknown, its marginal posterior density can be obtained via evaluating the identity $P(\boldsymbol{\sigma}^2) = P(\boldsymbol{\theta}, \boldsymbol{\sigma}^2)/P(\boldsymbol{\theta}|\boldsymbol{\sigma}^2)$ at $\boldsymbol{\theta} = 0$, where the numerator is given in (2.7) and the denominator is given by the conditional Normal distribution as discussed above. For ease of notation, we use $p(\cdot)$ as simplified notation for the posterior density $p(\cdot|\{y_{ij}\})$. In particular, noting that $P(0|\boldsymbol{\sigma}^2) \propto \sqrt{|\boldsymbol{\Omega}(\boldsymbol{\sigma}^2)|} e^{-\boldsymbol{\mu}^\top(\boldsymbol{\sigma}^2) \boldsymbol{\Omega}(\boldsymbol{\sigma}^2) \boldsymbol{\mu}(\boldsymbol{\sigma}^2)/2}$, $P(\boldsymbol{\sigma}^2)$ is proportional to

$$\prod_{i=1}^N \sigma_i^{-|J_i|-2-2\alpha} \frac{1}{\sqrt{|\boldsymbol{\Omega}(\boldsymbol{\sigma}^2)|}} \exp \left\{ \frac{1}{2} \boldsymbol{\mu}^\top(\boldsymbol{\sigma}^2) \boldsymbol{\Omega}(\boldsymbol{\sigma}^2) \boldsymbol{\mu}(\boldsymbol{\sigma}^2) - \sum_{i=1}^N \left[\frac{\sum_{j \in J_i} y_{ij}^2 + 2\beta}{2\sigma_i^2} + \frac{|J_i|\sigma_i^2}{8} \right] \right\}. \quad (2.11)$$

Because this is not a standard distribution, numerical methods are required. This can be done in multiple ways, such as applying an MCMC algorithm to sample $\{\mathbf{B}, \mathbf{G}, \boldsymbol{\sigma}^2\}$ jointly, or sampling

σ^2 from (2.11) via rejection sampling and $\{\mathbf{B}, \mathbf{G}\}$ from their conditional multivariate Gaussian distribution given σ^2 . Incidentally, a good rejection proposal density is a convenient independent-component inverse Gamma distribution found in the proof of the posterior propriety; see Appendix B.1. The latter strategy can be very effective, especially as it provides independent draws. However, it is less flexible when we extend the model, such as the log-t extension that we describe in Section 2.4. Consequently, we adopt the more flexible MCMC approach.

Since the dimension of the parameter space, $2N + M$, is typically large and the parameters are highly correlated, we use a Hamiltonian Monte Carlo (HMC) algorithm (Neal, 2011), which delivers a less correlated sample than do more traditional MCMC techniques (Metropolis et al., 1953; Hastings, 1970; Geman and Geman, 1984). We implement HMC using the **STAN** package in *Python* (Hoffman and Gelman, 2014; Stan Development Team, 2015, 2016), along with a blocked Gibbs sampler as an independent cross-check of **STAN**. In the blocked Gibbs sampling, we sample (\mathbf{B}, \mathbf{G}) jointly to improve mixing as opposed to one-at-a-time Gibbs sampling, thanks to the joint normality of (\mathbf{B}, \mathbf{G}) conditioning on σ^2 . See Appendix A for more details on both algorithms.

As is well known, computational efficiency for posterior sampling often is affected by modeling defects, such as near non-identifiability (e.g., Meng, 2018). Model (2.6) does not suffer from such a problem as long as τ_i is not too large compared to the magnitude of σ_i ; see Appendix B.2.

2.3 Building Intuition: Power Shrinkage and Variance Shrinkage

To communicate what our model aims to accomplish clearly and intuitively, we express its MAP estimators in terms of the usual linear shrinkage estimators (Efron and Morris, 1975; Morris, 1983) of B_i and G_j . As we shall see, these correspond to “power shrinkage” estimators on the original scale, i.e., A_i and F_j . Intuitively, shrinkage estimators combine information among all the instruments and sources as well as experts’ prior information through weighted averages, which serves well the purpose of calibration concordance across instruments and sources. Specifically, by setting the derivative of the log posterior in (2.7) with respect to \mathbf{B} and \mathbf{G} to be zero, we find that the MAP estimators conditional on $\boldsymbol{\tau}^2$, denoted by $\hat{B}_i(\boldsymbol{\tau}^2)$ and $\hat{G}_j(\boldsymbol{\tau}^2)$, must satisfy

$$\hat{B}_i(\boldsymbol{\tau}^2) = W_i(\bar{y}'_i - \bar{G}_i) + (1 - W_i)b_i, \quad \hat{G}_j(\boldsymbol{\tau}^2) = \bar{y}'_j - \bar{B}_i \quad (2.12)$$

where for notational simplicity we write $y'_{ij} = y_{ij} + 0.5\sigma_i^2$, suppressing the dependence on σ_i^2 . Here \bar{G}_i is the precision (i.e., the reciprocal of variance) weighted average of the $\hat{G}_j(\boldsymbol{\tau}^2)$ over $j \in J_i$ and \bar{B}_j is the precision weighted average of the $\hat{B}_i(\boldsymbol{\tau}^2)$ over $j \in J_i$, i.e.,

$$\bar{G}_i = \frac{\sum_{j \in J_i} \hat{G}_j(\boldsymbol{\tau}^2) \sigma_i^{-2}}{\sum_{j \in J_i} \sigma_i^{-2}} \quad \text{and} \quad \bar{B}_j = \frac{\sum_{i \in I_j} \hat{B}_i(\boldsymbol{\tau}^2) \sigma_i^{-2}}{\sum_{i \in I_j} \sigma_i^{-2}}.$$

Furthermore, $\bar{y}'_{i\cdot}$ is the precision weighted average of the y'_{ij} over $j \in J_i$, and $\bar{y}'_{\cdot j}$ is the precision weighted average of the y'_{ij} over $i \in I_j$, i.e.,

$$\bar{y}'_{i\cdot} = \frac{\sum_{j \in J_i} y'_{ij} \sigma_i^{-2}}{\sum_{j \in J_i} \sigma_i^{-2}} \quad \text{and} \quad \bar{y}'_{\cdot j} = \frac{\sum_{i \in I_j} y'_{ij} \sigma_i^{-2}}{\sum_{i \in I_j} \sigma_i^{-2}}.$$

Finally, the weights are

$$W_i = \frac{|J_i| \sigma_i^{-2}}{\tau_i^{-2} + |J_i| \sigma_i^{-2}} \quad (2.13)$$

and serve as the shrinkage factor for estimating B_i . The form of (2.13) is intuitive because it measures the relative precision (i.e., reciprocal of variance) provided by the likelihood with respect to the total posterior precision. Hence $1 - W_i$ is the proportion of information from the prior distribution. This metric permits us to make judicious choices of the prior variances $\{\tau_i^2\}$ when they are not given by the experts, so that our results would not be unduly prior-driven. See the applications in Sections 4.1, 4.2 and 4.3 for in-context discussion.

To illustrate the concept of “power shrinkage”, consider the case where $\boldsymbol{\tau}^2$ and $G_j = g_j$ are known. Then (2.12) yields

$$\hat{B}_i(\boldsymbol{\tau}^2) = W_i(\bar{y}'_{i\cdot} - \bar{g}_i) + (1 - W_i)b_i. \quad (2.14)$$

Consequently, the target Effective Area A_i is estimated by $\hat{A}_i(\boldsymbol{\tau}^2) = \exp[\hat{B}_i(\boldsymbol{\tau}^2)]$:

$$\hat{A}_i = \hat{A}_i(\boldsymbol{\tau}^2) = a_i^{1-W_i} \left[(\tilde{c}_i \tilde{f}_i^{-1}) e^{\sigma_i^2/2} \right]^{W_i} \quad (2.15)$$

where \tilde{c}_i and \tilde{f}_i are the geometric means:

$$\tilde{c}_i = \left[\prod_{j \in J_i} c_{ij} \right]^{1/|J_i|} \quad \text{and} \quad \tilde{f}_i = \left[\prod_{j \in J_i} f_j \right]^{1/|J_i|}. \quad (2.16)$$

This adjustment depends on the relative precision $1 - W_i$ for the b_i . If $W_i = 1$, that is, if b_i is not trustworthy at all, we just ignore a_i and estimate A_i by $\hat{A}_i = \left[\tilde{c}_i \tilde{f}_i^{-1} \right] e^{\sigma_i^2/2}$. Note that the bias

correction $e^{\sigma_i^2/2}$ is needed because otherwise $\tilde{c}_i \tilde{f}_i^{-1}$ converges to $A_i e^{-\sigma_i^2/2}$ as $|J_i| \rightarrow \infty$. In contrast, if $W_i = 0$, i.e., b_i possesses no error, then of course we ignore any data and just use $\hat{A}_i = a_i$ for A_i .

Because W_i grows with $|J_i| \sigma_i^{-2}$, for fixed σ_i^2 , the more calibration data we have, the larger the adjustment we should make. However, the precision is not determined by the *data size* $|J_i|$ alone, but also by the *quality* of the data, as reflected in σ_i^2 . Hence if both $|J_i|$ and σ_i^2 are large, W_i may not be near 1 because the indirect information $|J_i| \sigma_i^{-2}$ may not be large compared to τ_i^{-2} .

When $\{\sigma_i^2\}$ are unknown, we use independent conjugate prior distributions for $\{\sigma_i^2\}$ as in Section 2.2. Taking the derivative of the log of (2.7) with respect to σ_i^2 reveals that the MAP estimators also satisfy

$$\hat{\sigma}_i^2 = 2 \left[\sqrt{1 + S_{y,i}^2} - 1 \right], \quad S_{y,i}^2 = \frac{1}{|J_i| + \alpha} \left[\sum_{j \in J_i} (y_{ij} - \hat{B}_i - \hat{G}_j)^2 + \beta \right] \quad (2.17)$$

where β is the shape parameter for the inverse Gamma prior distribution for σ_i^2 as given in (2.6). We can simultaneously solve (2.12) and (2.17) to obtain the MAP estimators $\{\hat{\mathbf{B}}, \hat{\mathbf{G}}, \hat{\sigma}^2\}$. Heuristically, the consistency of $\hat{\sigma}_i^2$ can be seen by noting that, as $|J_i| \rightarrow \infty$, $S_{y,i}^2$ converges to the mean-squared error of $(y_{ij} - B_i - G_j)$, which is $\sigma_i^2 + [\sigma_i^2/2]^2$, and hence the expression for $\hat{\sigma}^2$ in (2.17) will converge to $2\sqrt{1 + \sigma_i^2 + [\sigma_i^2/2]^2} - 1 = \sigma_i^2$. For finite $|J_i|$, because $S_{y,i}^2 \geq \beta/(|J_i| + \alpha) \geq \beta/(M + \alpha)$, we know numerically all $\hat{\sigma}_i^2$ will be bounded below by $2\sqrt{1 + \beta/(M + \alpha)} - 2 > 0$. Hence our model, including its prior specifications, avoids a known problem of hierarchical modeling with variances becoming stuck at 0 because of too weak likelihood or prior information.

Intriguingly, the MAP estimator for the variance is also a shrinkage form because

$$\hat{\sigma}_i^2 = 2 \left[\sqrt{1 + S_{y,i}^2} - 1 \right] = \frac{2}{1 + \sqrt{1 + S_{y,i}^2}} S_{y,i}^2 \equiv R_i S_{y,i}^2 \quad (2.18)$$

where $S_{y,i}^2$ as defined in (2.17) is similar to the natural residual variance estimator for σ_i^2 , except for its incorporation of the prior information through $\{\alpha, \beta\}$. The half-variance correction leads to a shrinkage of $S_{y,i}^2$ because $R_i \leq 1$. The degree of shrinkage depends on $S_{y,i}^2$ itself. The larger $S_{y,i}^2$ is, the smaller R_i is, and hence the more shrinkage. To the best of our knowledge, such a self-weighted non-linear shrinkage phenomenon has not been studied in the literature.

2.4 Extensions to Handling Outliers: Log-t Model

The log-Normal model has a number of advantages as outlined above, but even after taking logarithms there may be substantial outliers. Outliers are not uncommon in astronomical observations because the harsh environments in which the detectors operate can be subject to large variations in background intensities, potentially leading to large errors in flux estimates. In addition, astronomical sources have intrinsic variabilities covering many orders of magnitude, and some measurements could be performed in regimes where the detectors do not respond linearly to the incoming signal. Here we propose a generalization of the log-Normal model by introducing a latent variable ξ_{ij} for each observation y_{ij} that is used to down-weight outliers for more robust inference.

Specifically, for any observation y_{ij} , we assume

$$\begin{aligned} y_{ij} \mid \mathbf{B}, \mathbf{G}, \boldsymbol{\xi} &= -\frac{\kappa^2}{2\xi_{ij}} + B_i + G_j + \frac{Z_{ij}}{\sqrt{\xi_{ij}}}, \\ Z_{ij} \mid \boldsymbol{\xi} &\stackrel{\text{indep}}{\sim} \mathcal{N}(0, \kappa^2), \quad B_i \stackrel{\text{indep}}{\sim} \mathcal{N}(b_i, \tau_i^2), \end{aligned} \quad (2.19)$$

where $\boldsymbol{\xi} = \{\xi_{ij}\}$. Because $E(e^{y_{ij}} \mid \mathbf{B}, \mathbf{G}) = E[E(e^{y_{ij}} \mid \mathbf{B}, \mathbf{G}, \boldsymbol{\xi}) \mid \mathbf{B}, \mathbf{G}] = A_i F_j$, the multiplicative model in (1.1) holds. Depending on assumptions about ξ_{ij} , (2.19) includes the following cases:

Case 1: log-Normal model with known variances. If the ξ_{ij} are known constants, the noise terms $e_{ij} = Z_{ij}/\sqrt{\xi_{ij}}$ are independent Gaussians with mean 0 and variance $\sigma_{ij}^2 = \kappa^2/\xi_{ij}$. Thus the model in (2.19) is equivalent to (2.6) with known variances.

Case 2: log-Normal model with unknown variances. If $\xi_{ij} = \xi_i \stackrel{\text{indep}}{\sim} \chi_u^2$ for all j , then the conditional variances of the noise terms $Z_{ij}/\sqrt{\xi_i}$, κ^2/ξ_i are distributed as independent scaled inverse χ^2 with degree of freedom u and scale $u\kappa^2$. Thus the model in (2.19) is equivalent to (2.6) with $\alpha = u/2, \beta = \kappa^2/2$ due to the equivalence of inverse χ^2 and inverse Gamma.

Case 3: log-t model. If $\xi_{ij} \stackrel{\text{indep}}{\sim} \chi_\nu^2$, i.e., mutually independent χ^2 random variables, which are also independent of the Z_{ij} , then the error terms $Z_{ij}/\sqrt{\xi_{ij}}$ follows independent (scaled) student-t distributions: $Z_{ij}/\sqrt{\xi_{ij}} \stackrel{\text{indep}}{\sim} (\kappa/\sqrt{\nu}) \text{ t}_\nu$.

The log-t model can also be fit using HMC via **STAN** in the package *CalConcordance*.

Besides down-weighting outliers, the latent variables ξ_{ij} also permit a unique variance κ^2/ξ_{ij} for each instrument-source combination. The log-t model is thus more flexible, but consequently

computationally more demanding, than the log-Normal model. The convergence of HMC is harder to achieve and the sampling is more costly. Another issue with the log-t model is that when the ξ_{ij} are small, the half variance corrections $\kappa^2/2\xi_{ij}$ tend to dominate the $Z_{ij}/\sqrt{\xi_{ij}}$, because of their (much) smaller denominator. This results in small y_{ij} , and hence the model tendency to generate heavier left tails than right tails, as seen in our simulation.

Despite these challenges, which are topics for further study, we will demonstrate the effectiveness of log-t compared with log-Normal for simulated and real data in the presence of serious outliers. Without outliers, however, the log-Normal model is adequately robust for real-world applications, especially when computational cost or numerical stability is of concern.

3 Testing the Concordance Models on Simulated Data

Through simulations, we aim to demonstrate that (1) the log-Normal approach is reasonably robust to the type of model specifications likely to occur in practice; (2) a commonly adopted plug-in method treating “guesstimated” variances as known can lead to very misleading adjustments; and (3) the log-t model is preferred in the presence of serious outliers.

3.1 Checking Robustness to Likely Misspecification

As discussed earlier, we approximate the Poisson counts via a log-Normal distribution and we pretend the T_{ij} are known without uncertainty in (1.1). These approximations have reasonable justifications (Marshall et al., 2017), but it is important to exercise our due diligence. Here we study the efficacy of the log-Normal approximation using simulation and leave more results (Simulations IV-VI) of the latter approximation and a combination of both to Appendix E.

In Simulations I and II, we assume that there are $N = 10$ instruments and $M = 40$ sources. The data are generated as $y_{ij} = \log \tilde{c}_{ij}$, where $\{\tilde{c}_{ij}\}$ are independent zero-modified Poisson counts with (respectively) $\lambda_{ij} = A_i F_j = \exp(B_i + G_j)$; see (2.3) for the mean and variance of \tilde{c}_{ij} . In Simulation I, we set $B_i = 1, G_j = 1$ but in Simulation II, $B_i = 5, G_j = 3$. We independently sample $b_i = \log a_i$ from $\mathcal{N}(B_i, \tau_i^2)$, where $\tau_i^2 = 0.05^2$ for each i . Thus Simulation I represents a low count scenario where the Normal approximation may not be appropriate. When σ^2 is treated as

known, e.g., a “guesstimated” value 0.1^2 , we use the posterior for B_i and G_j as given in Section 2.2. Otherwise, we specify their priors with independent inverse Gammas with degree of freedom $\alpha = 2$ and scale $\beta = 0.01$, and use HMC to obtain draws from the joint posterior distribution. These hyperparameter values are chosen to match astronomers’ prior knowledge; for example, 0.1^2 is the maximum of their “guesstimates” of $\{\sigma_i^2\}$, reflecting their general consensus that 10% or less relative error (recall y_{ij} is on log scale) does not alter physical interpretations in important ways. As expected, the fitted values of B_i and G_j are much closer to their targets in Simulation II since it has more Poisson counts resulting from larger values of B_i and G_j ; Figures 1 and 2 give detailed results (for B_i, σ_i) under Simulations I and II.

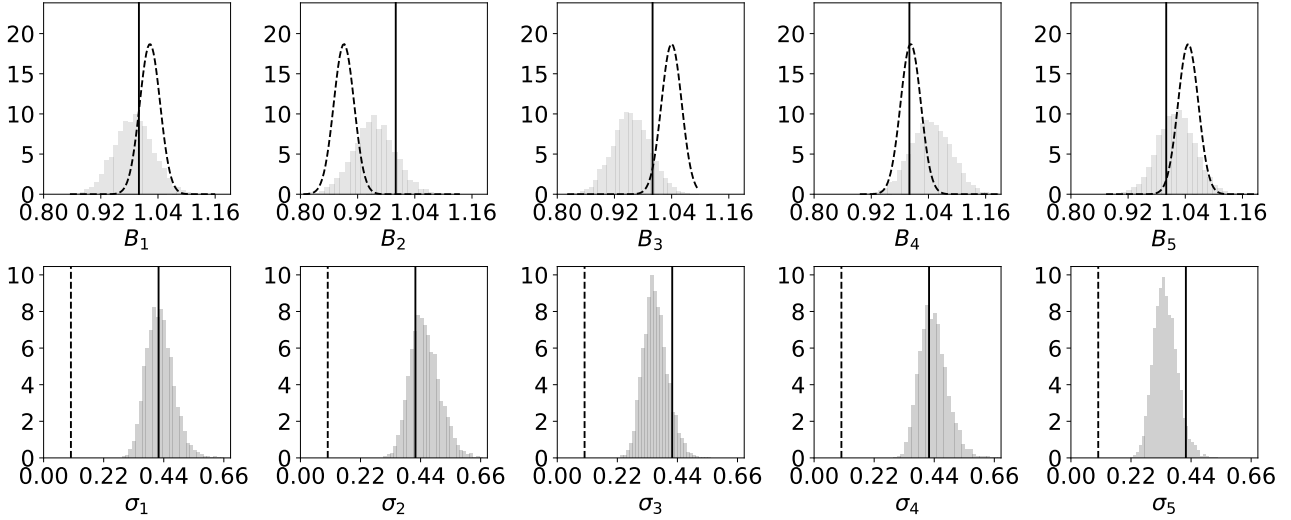


Figure 1: Simulation I. Posterior histograms of $\{B_i, \sigma_i\}_{i=1}^5$. The solid vertical black lines denote the true/theoretical values of $B_i = 1$ (top row) and of $\sigma_i = 0.421$ (second row). The dashed vertical lines denote $\sigma_i = 0.1$ (second row). The black dashed density curves denote the exact posterior densities of B_i when we set the variances equal to their “guesstimated” value $\sigma_i^2 = 0.1^2$.

Since \tilde{c}_{ij} is discrete, the theoretical variance of $\sigma_{ij}^2 = \text{Var}[\log(\tilde{c}_{ij})]$, which is a function of $\lambda = \exp(B_i + G_j)$, can be calculated numerically to any accuracy of our choice. For reasonably large $B_i + G_j$, we can also approximate σ_{ij}^2 by the δ -method: $\sigma_{ij}^2 \approx \text{Var}(\tilde{c}_{ij})/E^2(\tilde{c}_{ij})$, where $E(\tilde{c}_{ij})$ and $\text{Var}(\tilde{c}_{ij})$ are obtained from (2.3) with $\lambda = \exp(B_i + G_j)$. For Simulations I, $\lambda = e^2 = 7.4$, which leads to $\sigma_{ij} = 0.421$ by the numerical calculation; in contrast, the δ -method gives $\sigma_{ij} \approx 0.367$, a

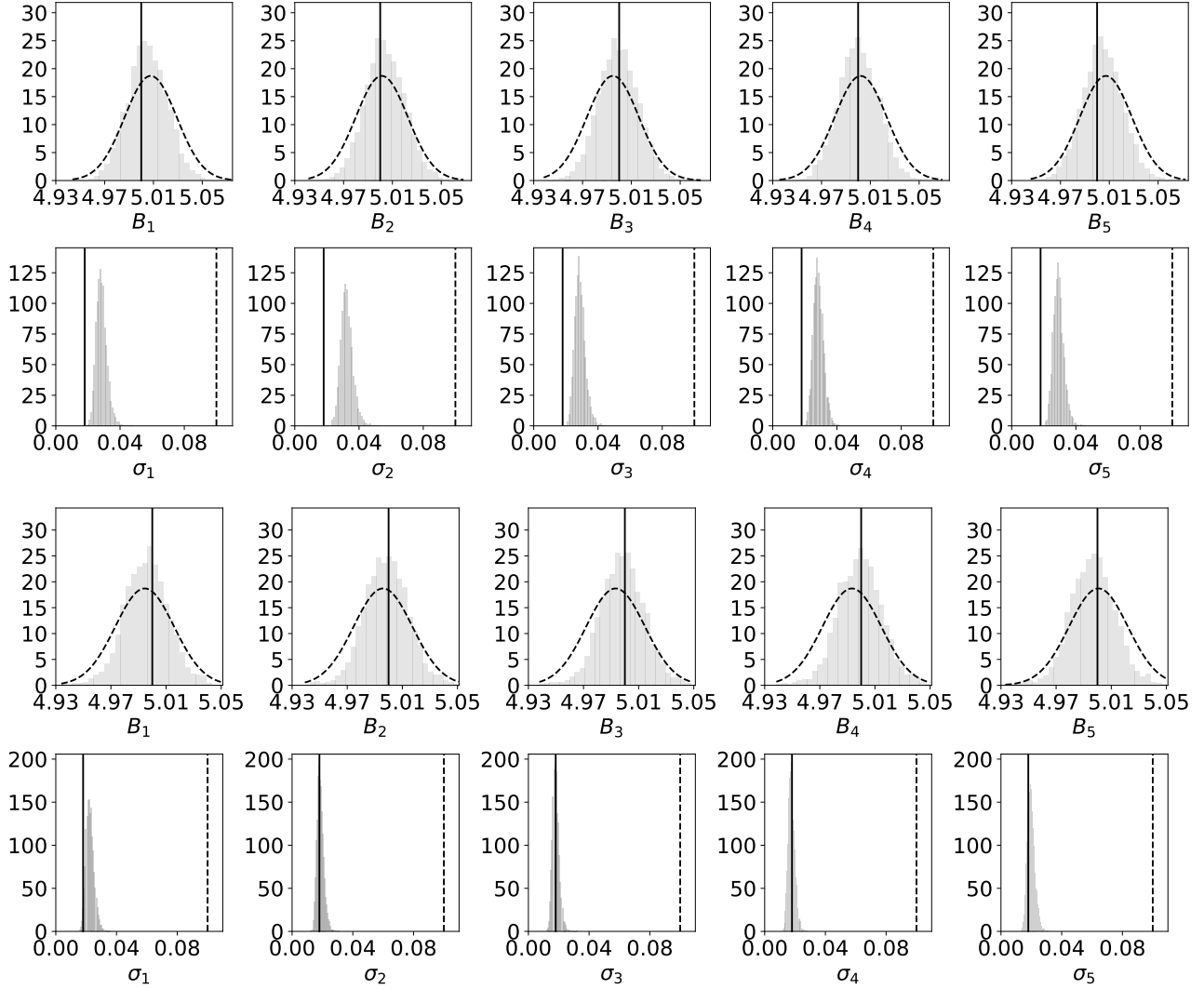


Figure 2: Simulation II. Posterior histograms of $\{B_i, \sigma_i\}_{i=1}^5$ corresponding to $\beta = 0.01$ (rows 1 & 2) and $\beta = 0.001$ (rows 3 & 4). The solid vertical black lines denote the true values of $B_i = 5$ (rows 1 & 3) and of $\sigma_i = 0.018$ (rows 2 & 4). The dashed vertical lines denote the “guesstimated” value $\sigma_i = 0.1$ (rows 2 & 4). The black dashed density curves in rows 1 & 3 denote the exact posterior densities of B_i when we set the variances equal to their “guesstimated” value $\sigma_i^2 = 0.1^2$.

poor approximation due to the smallness of λ . This serves also to warn us about the inadequacy of using the log-Normal approximation itself. In contrast, for Simulation II, $\lambda = e^8 = 2981$, and hence $\sigma_{ij} = 0.018$; the δ -method gives the same number (in terms of significant digits). Note that the priors for $\{\sigma_i^2\}$ are inverse Gammas with degrees of freedom 2 and scale β for both simulations; we use $\beta = 0.01$ for Simulation I, and $\beta = 0.01$ as well as $\beta = 0.001$ for Simulation II.

Now suppose a user inserts $\sigma_i^2 = 0.1^2$ as his or her “guesstimate” of the variances. Comparing the histograms and the overlaying curves from Figures 1 and 2, we see in Simulation I that the posterior distributions largely miss their targets, because $\sigma_i = 0.1$ is significantly smaller than the variances estimated under the unknown variance model. In contrast, when the former is larger than the latter, as in Simulation II, the posterior distribution of B_i does capture the target, except it possesses longer tails compared to the one with estimated variances. Both phenomena are expected, and they confirm again that, if one has to “guesstimate” the variances, it is wiser to err on the conservative side, because nothing is gained by having a posterior density precisely centered at a wrong location. Of course, larger variances imply less precision, which leads to less informative results, an inevitable (small) price for incorrectly specifying the variances.

3.2 Dealing with Outliers via log-t model

Simulation III, which is the same as Simulation II except for $G_1 = -2$ to induce outliers, demonstrates the effectiveness of the log-t model in dealing with outliers. Following notation in Case 3 of Section 2.4, setting the shape parameter for the inverse Gamma prior to be $\alpha = 2$ is the same as setting $\nu = 2\alpha = 4$ for χ_ν^2 ; the scale parameter $\beta = 0.01$ corresponds to $\kappa = \sqrt{2\beta} \approx 0.141$.

From Simulation II, $\sigma_{ij} = 0.018$ for $j > 1$. For $j = 1$, $\lambda = e^{-2+5} = 20.1$, and hence the exact numerical calculation gives $\sigma_{i1} = 0.232$, and the δ -method yields $\sigma_{i1} \approx 0.223$, quite a reasonable approximation. As discussed in Section 2.4, when the true $\{\sigma_{ij}^2\}$ for some sources are much larger than the others, the corresponding observations are likely, but not necessarily, to be outliers. Thus in this example, the observations from the first source are likely to be outliers.

Figure 3 compares, for the observations from the first three sources (just as an example), the fitted results from the log-Normal model and the log-t model through the (fitted) standardized

residuals, using the notation in Section 2.4:

$$\widehat{\mathcal{R}}_{ij} = \frac{y_{ij} - \widehat{B}_i - \widehat{G}_j + 0.5 \times \kappa^2 / \widehat{\xi}_{ij}}{\kappa / \widehat{\xi}_{ij}^{1/2}} \quad (3.1)$$

where $\widehat{B}_i, \widehat{G}_j, \widehat{\xi}_{ij}$ are the posterior means. Using the notation for the log-Normal hierarchical model in Section 2.2, $\widehat{\mathcal{R}}_{ij}$ can be expressed as

$$\widehat{\mathcal{R}}_{ij} = \frac{y_{ij} - \widehat{B}_i - \widehat{G}_j + 0.5 \times \widehat{\sigma}_i^2}{\widehat{\sigma}_i} \quad (3.2)$$

where, again, $\widehat{B}_i, \widehat{G}_j, \widehat{\sigma}_i$ are the posterior means. Some observations from the first source (black circles) appear to be outliers, with standardized residuals lying outside the $[-2, 2]$ interval, in the log-Normal model (upper panel) but not for the log-t model (lower panel). In the log-Normal model, setting $\sigma_{ij}^2 = \sigma_i^2$ causes failure due to some source-dependent large variances: $\sigma_{i1}^2 \gg \sigma_{ij}^2$, $j \geq 2$. In the log-t model, the outliers are down weighted by the latent variables ξ_{ij} and each observation is assigned its unique conditional variance $\sigma_{ij}^2 = \kappa^2 / \xi_{ij}$. This indicates that log-t model is more capable of handling outliers than the log-Normal model.

Figure 4 shows the posterior distributions of B_i by the log-Normal model and log-t model, and both models capture the true value. It is rather comforting that the results from the log-t model have only slightly larger variance than those from the log-Normal model, considering the log-t model is much more flexible, by allowing individual σ_{ij} via “soft prior constraints” instead of the hard-constraint $\sigma_{ij} = \sigma_i$ as imposed by the log-Normal model.

Nevertheless, we compare the actual coverage properties of log-Normal and log-t through simulations to investigate if the increased posterior-interval width of the latter approach is necessary, from a frequentist evaluative perspective. The first three rows of Table 1 give the (average) actual coverage probabilities of nominal 95% posterior intervals (formed by the 2.5% and 97.5% percentiles) for B_i and G_j obtained from 2000 repeated simulations, with the same configurations as in Simulation III. As approximations to Poisson models, the log-t model is more robust than the log-Normal model for outliers, producing significantly better – though still very poor compared to the nominal level – coverage probability for G_1 . Table 1 also indicates that the presence of outliers is not as problematic for estimating B_i , our primary interest, as that for G_1 . This is because we are more “informed” about the B_i than the G_j for two reasons: (1) in this experiment

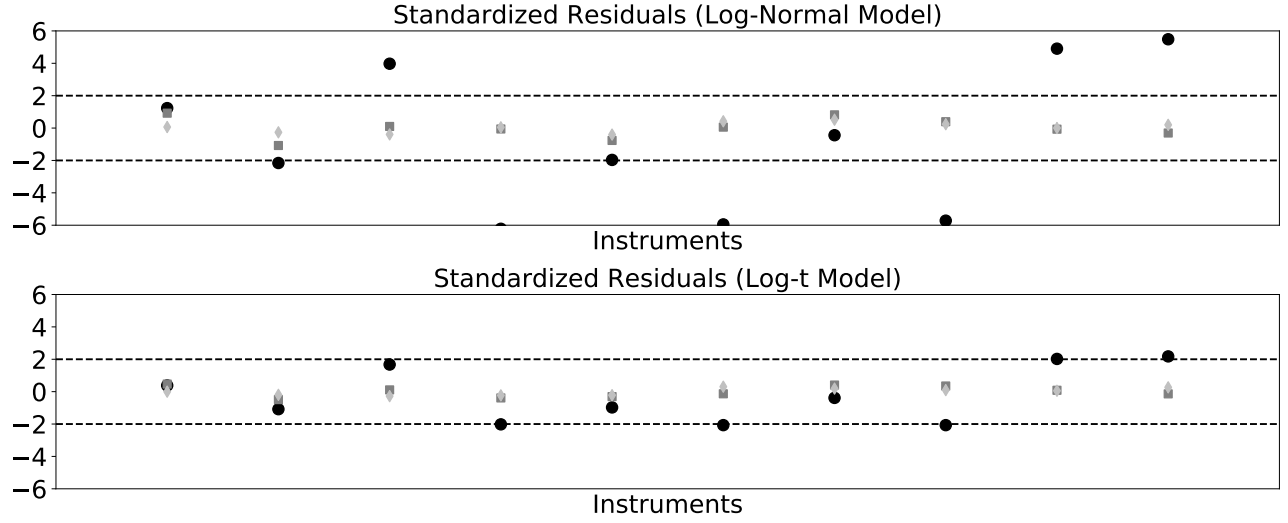


Figure 3: Simulation III. Standardized residuals of the log-Normal hierarchical model (upper panel) and the log-t model (lower panel). The black circles, gray squares and silver rhombi represent the first three sources respectively. The instruments are plotted on the x-axes. The dashed horizontal lines denote the $[-2, 2]$ intervals.

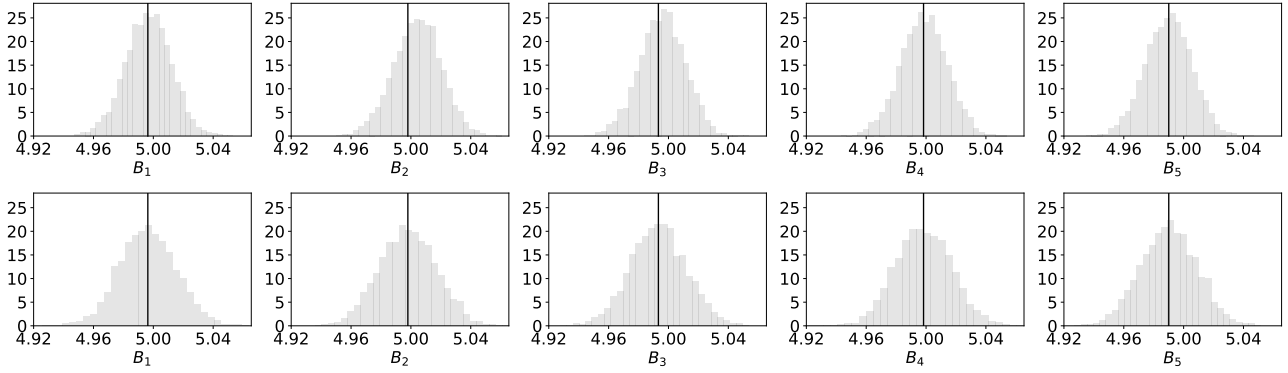


Figure 4: Simulation III. Posterior histograms of $\{B_i\}_{i=1}^5$ from the log-Normal hierarchical model (upper panel) and the log-t model (lower panel), where the black lines indicate the true value.

Data Generating Model (Poisson)	Parameter	Coverage Probability		Length of Interval	
		log-Normal	log-t	log-Normal	log-t
$N = 10, M = 40$	\mathbf{B}	[0.941, 0.959]	[0.971, 0.975]	0.067±0.005	0.073 ± 0.002
$N = 10, M = 40$	G_1	0.399	0.700	0.090± 0.015	0.182±0.045
$N = 10, M = 40$	G_2, \dots, G_M	[0.967, 0.977]	[0.996, 0.999]	0.077±0.003	0.104±0.002
$N = 40, M = 40$	\mathbf{B}	[0.953, 0.969]	[0.993, 0.998]	0.041±0.007	0.050±0.001
$N = 40, M = 40$	G_1	0.398	0.686	0.045±0.003	0.093±0.013
$N = 40, M = 40$	G_2, \dots, G_M	[0.965,0.977]	[0.996,0.999]	0.038±0.001	0.051±0.001

Table 1: Coverage probabilities of 95% posterior intervals calculated from 2000 repeated simulations when the data generating model is Poisson, under the same configurations as in Simulation III. The intervals $[\cdot, \cdot]$ in columns 3 & 4 give the smallest and largest values of the coverage probabilities corresponding to parameters in the second column. The last two columns give the lengths of 95% intervals in the format of mean \pm standard deviation.

$N = 10, M = 40$, and thus there are more sources than instruments, and (2) each B_i has an informative prior whereas the G_j has only a flat prior.

As seen in Table 1, when N is increased from 10 to 40, the coverage probabilities for \mathbf{G} remain very similar. But the coverage probabilities for \mathbf{B} go up noticeably, especially under the log-t model, yet all intervals become much narrower. The narrowing of the intervals for \mathbf{G} is expected with more instruments per source. The simultaneous increase of confidence coverage and decrease of interval-widths for \mathbf{B} is an intriguing phenomenon. It is a welcome finding from the astrophysics application perspective. But it also indicates potential defects in log-Normal or log-t approximations because the over-coverage suggests that the model is not calibrating posterior uncertainties in the most efficient way. The half-variance correction likely plays a complicated role here because it permits uncertainty in variance estimation to directly affect inference about the mean. Overall, our finding is that the log-t approach is recommended if one suspects the presence of serious outliers. This will lead to some perhaps unnecessarily larger uncertainty bars for flux estimates that are not (directly) affected by the outliers, but this might be a worthwhile premium against disastrous loss of coverage for those that are affected.

4 Applying the Proposed Methods to IACHEC Data

In this section, we fit the log-Normal hierarchical model to three data sets compiled by researchers from IACHEC (2017), with the aim to understand calibration properties of various X-ray telescopes (a.k.a., instruments) such as *Chandra*, *XMM-Newton*, *Suzaku*, *Swift*, etc. See Marshall et al. (2017) for detailed descriptions of the data collection and preprocessing processes.

4.1 E0102 Data

SNR 1E 0102.2-7219 (popularly abbreviated E0102), a calibration target for a variety of X-ray missions, is the remnant of a supernova that exploded in a neighboring galaxy known as the Small Magellanic Cloud (Chandra X ray observatory, 2009). We consider four photon sources associated with E0102. Each of the sources is a local peak or “line” that appears in the E0102 spectrum, which can be thought of as a high-resolution histogram of the energies of photons originating from E0102. That is, we consider the photon counts in four bins of this histogram. Two of the lines are associated with highly ionized Oxygen (Hydrogen Lyman- α like O VIII at 18.969Å and the resonance line of O VII from the He-like triplet at 21.805Å) and the other two are associated with Neon (H-like Ne X at 12.135Å and He-like resonance line Ne IX at 13.447Å). We consider replicate data obtained with 13 different detectors configurations respectively over 4 separate telescopes, *Chandra* (HETG and ACIS-S), *XMM-Newton* (RGS, EPIC-MOS, EPIC-pn), *Suzaku* (XIS), and *Swift* (XRT). Details of how the spectra are preprocessed to obtain relevant line counts can be found in Plucinsky et al. (2017).

Because the energies of the two O lines are similar, it is reasonable to assume that the associate Effective Areas are also similar; likewise for the Neon lines and their Effective Areas. That is, by considering two separate data sets, one with O VII and O VIII and the other with Ne IX and Ne X each hence with $M = 2$ and $N = 13$ (number of detectors), we have more confidence in the multiplicative model (1.1) than when we treat it as a single dataset with $M = 4$ and $N = 13$. In addition, standard astronomical practice is to work with dimensionless measurements in log space (e.g., optical magnitudes in a given passband are defined as $-2.5 \log_{10} \frac{\text{flux}}{\text{flux from Vega}}$). Since our log transformation of brightness mimics this process, we also normalize the measured line fluxes by those from an arbitrarily chosen detector, as done in Plucinsky et al. (2017).

To apply the log-Normal model (2.6) to the two data sets, we choose the hyperparameters as $\alpha = 1.5$, $\beta = 0.014^2$ for O VII, O VIII and $\alpha = 1.5$, $\beta = 0.009^2$ for Ne IX, Ne X. We set each $b_i = 0$, i.e., a priori we expect no adjustment is needed, with confidence τ_i , with two possible values $\tau_i = 0.025$ and $\tau_i = 0.05$. All these (and subsequent) choices are made according to the empirical knowledge of astronomers, and their interests in the kind of values they wish to test.

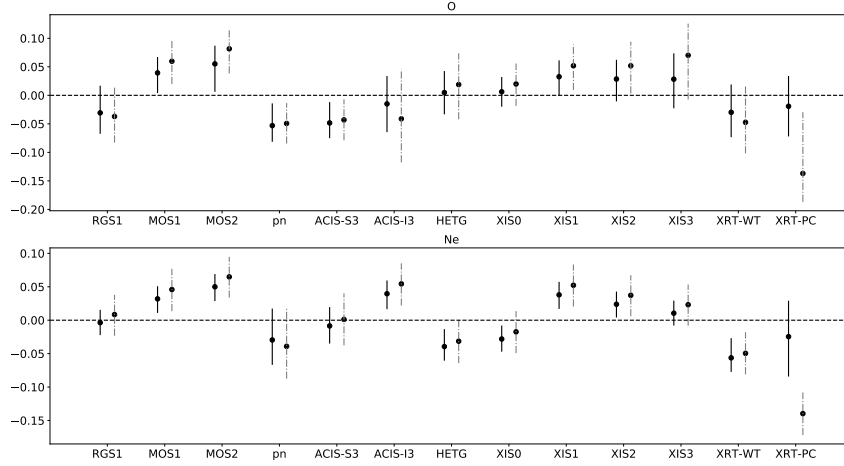


Figure 5: Adjustments of the log of the Effective Area for O (row 1) and Ne (row 2) in the E0102 data set. The x-axis labels the detectors and the y-axis is B_i . The horizontal dashed lines represent zero, the baseline. The vertical bars denote 95% posterior interval for each B_i , and the dots for the posterior means. The black and gray bars correspond to $\tau_i = 0.025$ and 0.05 , respectively.

Figure 5 shows the adjustments of the log-scale Effective Area for O (row 1) and Ne (row 2) in the E0102 data set. We see that the estimated values of B_i are not sensitive to the choices of τ_i except for detector XRT-PC. For XRT-PC, with the Ne data, the estimated shrinkage factor W of (2.13) is 0.91 when $\tau_i = 0.025$ and 0.02 when $\tau_i = 0.05$. This indicates that, when the prior variance of B_i is too small ($\tau_i = 0.025$ here), the model treats the observations as being less accurate (by fitting a large σ_i) instead of adjusting the Effective Area of the corresponding instrument more (a larger deviation from b_i). Table 2 reveals that the estimated shrinkage factors can vary slightly or drastically with τ_i . Since the number of sources is very small ($M = 2$), sensitivity to the choice of hyperparameters should not come as a surprise. But a unique feature of the log-Normal model is the direct link between its mean and variance because of the half-variance correction, which can

induce additional sensitivities that are not commonly observed (and hence not well studied).

Instrument	O		Ne	
	$\tau = 0.025$	$\tau = 0.05$	$\tau = 0.025$	$\tau = 0.05$
RGS1	0.570	0.205	0.063	0.016
MOS1	0.279	0.077	0.075	0.019
MOS2	0.355	0.065	0.077	0.017
pn	0.250	0.041	0.620	0.218
ACIS-S3	0.218	0.040	0.270	0.088
ACIS-I3	0.906	0.640	0.099	0.026
HETG	0.648	0.341	0.129	0.034
XIS0	0.180	0.051	0.069	0.018
XIS1	0.298	0.078	0.071	0.019
XIS2	0.463	0.140	0.063	0.016
XIS3	0.772	0.364	0.062	0.018
XRT-WT	0.726	0.278	0.154	0.026
XRT-PC	0.934	0.235	0.906	0.017

Table 2: Proportion of prior influence, as defined by $1 - W$ (of (2.13)), for E0102 data in Section 4.1.

For example, from Figure 5 and Table 2, XRT-PC has a much lower Effective Area than other instruments: about -0.15 versus between $[-0.05, 0.05]$ on the log scale. The corresponding estimated shrinkage factor is more sensitive to the choice of τ_i , for both O and Ne data: when τ_i is small ($= 0.025$), the mean is constrained too much by the prior density centered at zero, thus we need a larger σ_i to compensate for the bias in means. In contrast, when τ_i is larger (we tried $0.05, 0.075, 0.1$), the estimated shrinkage factor is no longer as sensitive to τ_i . Overall, Figure 5 suggests that the Effective Areas of MOS1, MOS2, XIS1, XIS2, XIS3 need to be adjusted downward and those of pn, XRT-WT, XRT-PC need to be adjusted upward.

4.2 2XMM Data

The 2XMM catalog can be used to generate large, well-defined samples of various types of astrophysical objects, notably active galaxies (AGN), clusters of galaxies, interacting compact binaries, and active stellar coronae, using the power of X-ray selection (XMM Catalogue public pages, 2008). The 2XMM data come from the XMM-Newton European Photon Imaging Cameras (EPIC). Briefly, there are three EPIC instruments: the EPIC-pn (hereafter referenced as “pn”) and the two EPIC-MOS detectors (hereafter referenced as “MOS1” and “MOS2”). These detectors have separate X-ray focusing optics but are co-aligned so that the sources in our samples are observed simultaneously in the pn, MOS1, and MOS2 detectors.

The 2XMM data contain three data sets, corresponding to the hard (2.5 - 10.0 keV), medium (1.5 - 2.5 keV) and soft (0.5 - 1.5 keV) energy bands. The three detectors (pn, MOS1 and MOS2) measured 41, 41, and 42 sources respectively in hard, medium, and soft bands. The sources are from the 2XMM EPIC Serendipitous Source Catalog (Watson et al., 2009), selected to be sufficiently faint that the thorny issue of “pileup”, which occurs when several photons hit the detector at the same time, can be ignored. With sufficient exposure, on average 1,500 counts are collected from the faint sources in each band for each detector (Marshall et al., 2017).

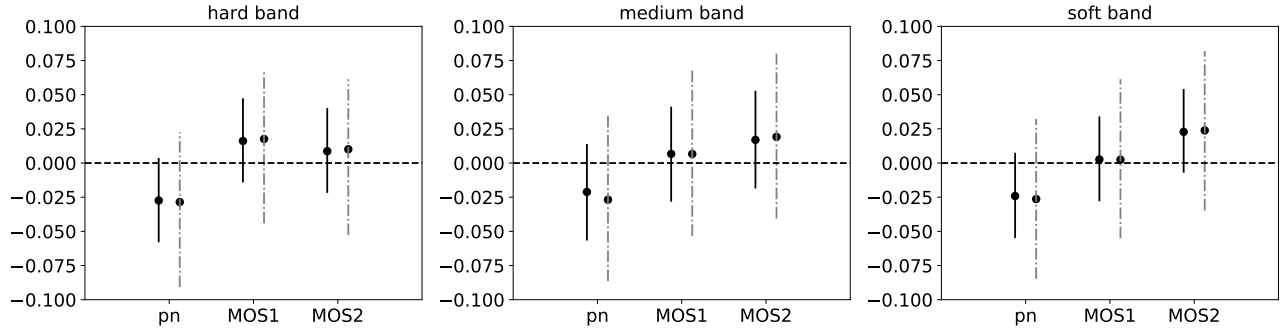


Figure 6: Adjustments of the log-scale Effective Areas for hard band (left), medium band (middle) and soft band (right) of the 2XMM data sets. The legend is the same as in Figure 5.

Data Name	$\tau_i = 0.025$			$\tau_i = 0.05$		
	pn	mos1	mos2	pn	mos1	mos2
hard band 2XMM	0.093	0.075	0.082	0.025	0.020	0.022
medium band 2XMM	0.250	0.216	0.222	0.076	0.065	0.067
soft band 2XMM	0.093	0.075	0.069	0.025	0.020	0.018
hard band XCAL	0.010	0.019	0.031	0.003	0.005	0.008
medium band XCAL	0.023	0.016	0.028	0.006	0.004	0.007
soft band XCAL	0.021	0.011	0.007	0.005	0.003	0.002

Table 3: Proportion of prior influence for data in Section 4.2 and 4.3.

The log-Normal hierarchical model (2.6) is fit to the three data sets separately, with $\beta = 0.116^2, 0.288^2$ and 0.148^2 respectively for the hard, median, and soft bands, but with the same $\alpha = 1.5$. We again use $b_i = 0$ and try $\tau_i = 0.025$ and $\tau_i = 0.05$. Figure 6 shows the resulting adjustments of the log-scale Effective Area, and they confirm the astronomers’ expectation that no adjustment are needed for 2XMM data, regardless of the choice of the τ_i . We tabulate the proportion of prior information for each detector-source pair for 2XMM data (as well as for XCAL data in Section 4.3) in Table 3, which shows a much more stable pattern compared to Table 2.

4.3 XCAL Data

Another XMM data set consists of bright active galactic nuclei from the XMM-Newton cross-calibration sample, denoted by “XCAL”.¹ The “pileup” issue cannot be ignored for XCAL data, so the image data are clipped to eliminate the regions affected by pileup and the estimated effective area is adjusted according to lookup tables (from other in-flight data) that account for the unused regions. The region that is clipped out is determined using a standard XMM software task (called `epatplot`) and depends on the observed source intensity: unused regions are larger for brighter sources (Marshall et al., 2017). Like the 2XMM data, XCAL data are composed of three datasets: the hard (94 sources), medium (103), and soft (108) bands, all measured by three detectors, MOS1,

¹See Section 4 of XMM-SOC-CAL-TN-0052 (available at <http://xmm2.esac.esa.int/docs/documents/CAL-TN-0052.ps.gz>)

MOS2 and pn. The model fitting uses the same procedure and hyperparameters as in Section 4.2, except with $\beta = 0.028^2, 0.093^2$ and 0.026^2 respectively for hard, median, and soft bands.

Figure 7 demonstrates that adjustment of the Effective Areas is needed to make the measured fluxes consistent across different detectors. We take four sources from the medium band data and use black vertical bars to denote the 95% intervals (mean ± 2 given standard deviations) for the log-fluxes obtained with a standard astronomical method for each of the three detectors. The intervals match in some cases but are quite distinct in others. For each source, we also plot our 95% posterior intervals of the estimated log-fluxes after adjustment using the log-Normal hierarchical model. The fitting results with different τ_i are consistent, regardless of the length of the posterior interval. This simple visualization gives us evidence that calibration of the Effective Areas is reliable, and more importantly necessary, to obtain consistent flux estimates.

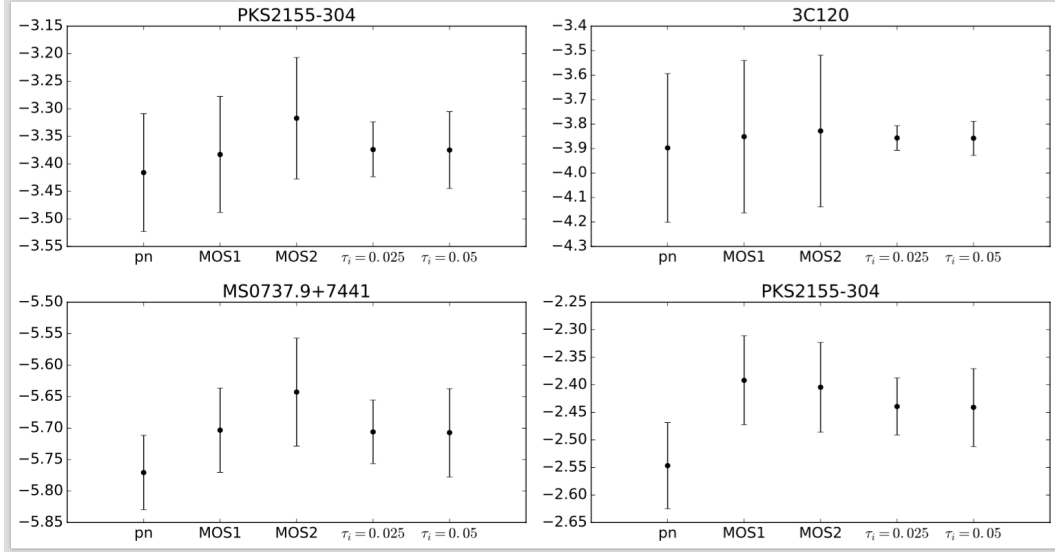


Figure 7: Comparison of estimated 95% intervals for log-fluxes using a standard astronomical method (left three bars) and those from the log-Normal hierarchical model (right two bars) for four representative sources in medium band, as indicated by the panel titles.

Finally, we show how to adjust the Effective Areas of each instrument to obtain the results illustrated in the rightmost interval in each panel of Figure 7. Figure 8 shows the necessary adjustment of the B_i for hard band (left), medium band (middle) and soft band (right). For all these bands, we must adjust pn upward and MOS2 downward.

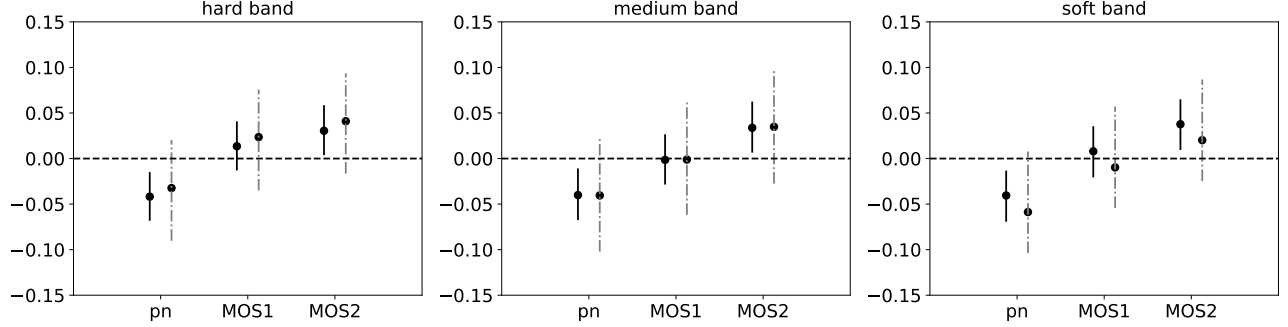


Figure 8: Adjustments of the log-scale Effective Areas for hard band (left), medium band (middle) and soft band (right) for XCAL data. The legend is the same as in Figure 5.

4.4 Model Checking

In this section, we check how well the log-Normal hierarchical model captures the observed variability in the data. We use residual plots to visualize the goodness-of-fit. Specifically, Figure 9 plots the standardized residuals $\hat{\mathcal{R}}_{ij}$ for data analyzed in Section 4.3 with $\tau_i = 0.05$, with the left panel denoting residuals from the log-Normal model ($\hat{\mathcal{R}}_{ij}$ defined in (3.2)) and the right panel the residuals from the log-t model ($\hat{\mathcal{R}}_{ij}$ defined in (3.1)). Nearly all residuals fall in $[-3, 3]$ for log-Normal and $[-2, 2]$ for log-t. The observations of 3C111 in all three energy bands are the only outliers for log-Normal but not for log-t, confirming the latter’s ability to handle outliers. The adjusted Effective Areas and the estimated fluxes are not too sensitive to whether or not the outliers are excluded. Thus the log-Normal model is reasonable for the data in Section 4.3.

We also employ a posterior predictive check (Meng, 1994; Gelman et al., 1996) for the log-Normal model. In a posterior predictive check, one chooses test statistics and computes the corresponding posterior predictive p-value. The test statistics we choose are

$$\left\{ T_i = \bar{y}_{i\cdot} - \bar{y} = \frac{\sum_{j=1}^M y_{ij}}{M} - \frac{\sum_{i=1}^N \sum_{j=1}^M y_{ij}}{NM} \right\}_{i=1}^N,$$

which reflect the relative magnitudes of the log scale Effective Areas. None of the posterior predictive p-values for any of our datasets are significant, i.e., we never fail the posterior predictive check. This by no means implies that no serious model defects exist. Below we discuss directions for improving our models and ultimately the reliability of the concordance adjustments they propose.

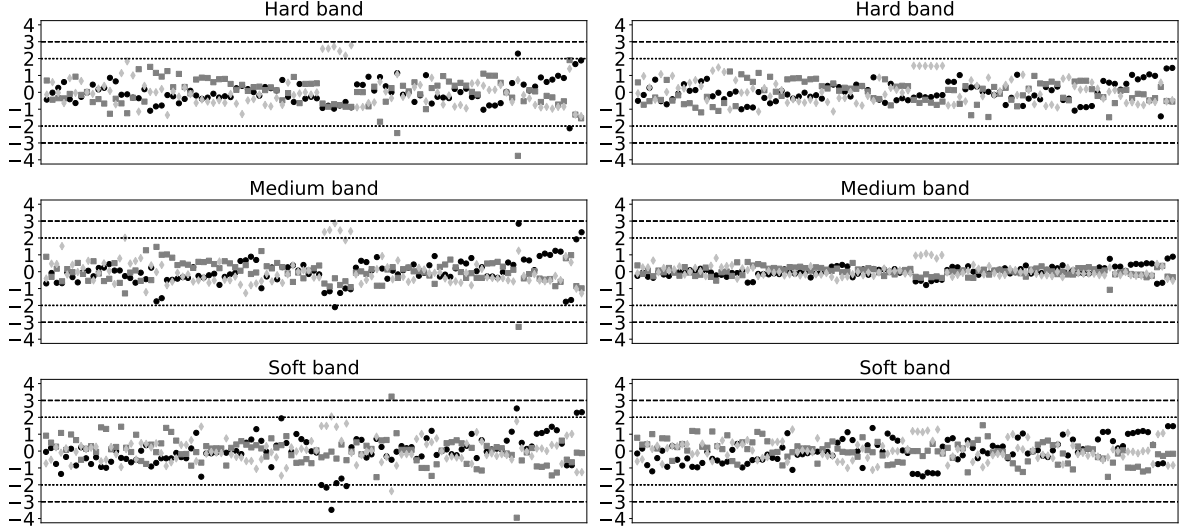


Figure 9: Standardized residuals for the data in Section 4.3 with $\tau_i = 0.05$, the log-Normal hierarchical model on the left panel and log-t model on the right panel. The black circles, gray squares and silver rhombi denote the instruments pn, MOS1 and MOS2 respectively. The dashed horizontal lines denote the $[-3, 3]$ intervals and the horizontal dots denote $[-2, 2]$ intervals.

5 Alternative Methods and Future Work

5.1 Comparing Likelihood and Bayesian Estimations

In Section 2, we adopt a Bayesian perspective, which leads to the log-Normal hierarchical model elaborated in Sections 2 and 4. But we can also treat (2.2) and (2.4) as a multivariate linear regression model, and fit it via maximum likelihood estimation. In particular, when all the variances in σ^2 are known, this is just a multivariate Gaussian model. Proposition 1 in Appendix D.1 gives closed-form solution of the variance-covariance matrix for the MLEs of $\{\mathbf{B}, \mathbf{G}\}$ when all the instruments measure all sources, which implies the asymptotic properties of the MLEs given in Corollary 1. Furthermore, the standardized residual sum of squares follow a χ^2 distribution, which enables easy testing of the goodness-of-fit; see Appendix D.2 for details.

When the variances σ^2 are unknown, in principle, we can still obtain the (asymptotic) variance of the MLEs by calculating the observed/expected Fisher information. However, the number of unknown parameters we consider, $2N + M$, grows without bound as the number of observations

$NM + N$ goes to infinity. Consequently, we cannot rely on standard asymptotic theory without carrying out the actual proof (as we did when σ^2 is known). Conditions on the relationship between N and M that would still ensure the classical asymptotic theory for MLEs should be of interest to those who prefer likelihood inference. Furthermore, under such conditions, these estimators should be *approximately* valid even if the Gaussian assumptions made in (2.2) for the b_i are not valid. In this case, the variance of the estimator requires a more complicated “sandwich” formula, involving both the Fisher information and the variance of the score function. Here we say *approximately* valid because the half-variance correction of Section 2 would still depend on the log-Normal assumption. Consequently, when the variance is large, our bias correction can be misleading if the log-Normal assumption is severely violated.

As usual, the likelihood method is closely related to the Bayes approach. For example, when σ^2 is known, the MLEs of the B_i and the G_j correspond to the MAP estimation defined in (2.12), which also have the intuitive interpretation as shrinkage estimators. When the variances are unknown, the likelihood function is unbounded at the boundary of the parameter space ($\sigma_i^2 = 0$). The conjugate priors for variance parameters in the Bayesian model regularizes the likelihood and gives a proper posterior distribution. This is another reason we adopt the Bayesian recipe.

5.2 Future Work

The log-Normal model works reasonably well for a number of real datasets provided to us, and it yields important findings that are welcomed by astronomers — concrete guidance about systematic adjustments of the Effective Areas are given and thus concordance of an intrinsic characteristic of each astronomical object across different instruments can be achieved. Calibration scientists are thus able to make *absolute* measurements of characteristics of astronomical objects using different instruments. Furthermore, we highlight the danger of incorrectly fixing the observation noise through various simulation experiments that mimic possible realistic uncertainties.

There are several directions of future work in order to improve the current model. First, so far we have assumed that the Effective Areas are a priori independent, which is not always true in practice. Sometimes the Effective Areas across different energy bands are noticeably correlated. This correlation structure needs to be taken into account in future modeling to gain

more efficiency in estimation. Second, the log-Normal model gives conservative results under realistic model misspecification, as revealed by our simulation studies. But the scope of simulation studies is always too limited. Hence theoretical properties of the log-Normal approach under model misspecification need to be further investigated, and similarly for the log-t model. Last, the asymptotic (sampling) properties of the proposed models need to be established, as both the number of parameters and the number of observations approach infinity.

More generally, we believe our general modeling strategies can be adopted to conduct similar concordance analysis for other instruments, such as for environmental monitoring (e.g., Weatherhead et al., 1998). We invite interested readers to pursue such applications.

References

- Chandra X ray observatory (2009). E0102-72.3: Adding a new dimension to an old explosion. <http://chandra.harvard.edu/photo/2009/e0102/>.
- Drake, J. J., Ratzlaff, P., Kashyapa, V., Edgara, R., Izemb, R., Jeriusa, D., Siemiginowskaa, A., and Vikhlinina, A. (2006). Monte Carlo processes for including Chandra instrument response uncertainties in parameter estimation studies. In *SPIE Astronomical Telescopes + Instrumentation*, pages 62701I–62701I. International Society for Optics and Photonics.
- Efron, B. and Morris, C. N. (1975). Data analysis using Stein’s estimator and its generalizations. *Journal of the American Statistical Association*, 70(350):311–319.
- Gelman, A., Meng, X.-L., and Stern, H. (1996). Posterior predictive assessment of model fitness via realized discrepancies. *Statistica Sinica*, 6(4):733–760.
- Geman, S. and Geman, D. (1984). Stochastic relaxation, Gibbs distributions, and the Bayesian restoration of images. *IEEE Transactions on Pattern Analysis and Machine Intelligence*, 6:721–741.
- George, I. M., Arnaud, K. A., Pence, B., and Ruamsuwan, L. (1992). Calibration sources for spectral analysis. *Legacy*, 2.
- Graessle, D. E., Evans, I. N., Glotfelty, K., He, X. H., Evans, J. D., Rots, A. H., Fabbiano, G., and Brissenden, R. J. (2006). The Chandra X-ray observatory calibration database (CalDB): building, planning, and improving. *Proc. SPIE*, 6270:62701X–62701X–12.
- Guainazzi, M., David, L., Grant, C. E., Miller, E., Natalucci, L., Nevalainen, J., Petre, R., and Audard, M. (2015). On the in-flight calibration plans of modern X-ray observatories. *Journal of Astronomical Telescopes, Instruments, and Systems*, 1(4):047001.
- Hastings, W. (1970). Monte Carlo sampling methods using Markov chains and their applications. *Biometrika*, 57(1):97–109.

- Hoffman, M. D. and Gelman, A. (2014). The No-U-Turn sampler: Adaptively setting path lengths in Hamiltonian Monte Carlo. Journal of Machine Learning Research, 15(1):1593–1623.
- IACHEC (2017). International Astronomical Consortium for High Energy Calibration. <http://web.mit.edu/iachec/>.
- Kashyap, V., Lee, H., Siemiginowska, A., McDowell, J., Rots, A., Drake, J., Ratzlaff, P., Zezas, A., Izem, R., Connors, A., and van Dyk, D. (2008). How to handle calibration uncertainties in high-energy astrophysics. Proceedings of SPIE (Observatory Operation: Strategies, Processes, and System II), 7016:23 (8pp).
- Lee, H., Kashyap, V. L., Van Dyk, D. A., Connors, A., Drake, J. J., Izem, R., Meng, X.-L., Min, S., Park, T., Ratzlaff, P., and Siemiginowska, A. (2011). Accounting for calibration uncertainties in X-ray analysis: effective areas in spectral fitting. The Astrophysical Journal, 731(2):126 (19pp).
- Madsen, K. K., Beardmore, A. P., Forster, K., Guainazzi, M., Marshall, H. L., Miller, E. D., Page, K. L., and Stuhlinger, M. (2016). IACHEC cross-calibration of Chandra, Nustar, Swift, Suzaku, XMM-Newton with 3C 273 ANDPKS 2155-304. The Astronomical Journal, 153(1):2(17pp).
- Marshall, H., Kashyap, V., Chen, Y., Meng, X.-L., and Wang, X. (2017). Concordance: In-flight calibration of X-ray telescopes without absolute references. In Preparation.
- Matthews, G. and Havey, Jr., K. (2010). Ten years of Chandra: reflecting back on engineering lessons learned during the design, fabrication, integration, test, and verification of NASA’s great X-ray observatory. Proc. SPIE, 7738:77380Y–77380Y–13.
- Meng, X.-L. (1994). Posterior predictive p-values. The Annals of Statistics, 22(3):1142–1160.
- Meng, X.-L. (2018). Conducting highly-principled data science: A statistician’s job and joy. Statistics and Probability Letters. To appear.
- Metropolis, N., Rosenbluth, A., Rosenbluth, M., Teller, A., and Teller, E. (1953). Equations of state calculations by fast computing machines. Journal of Chemical Physics, 21(6):1087–1092.
- Morris, C. N. (1983). Parametric empirical Bayes inference: theory and applications. Journal of the American Statistical Association, 78(381):47–55.
- Neal, R. M. (2011). MCMC using Hamiltonian dynamics. In Brooks, S., Gelman, A., Jones, G., and Meng, X.-L., editors, Handbook of Markov chain Monte Carlo, volume 2. CRC Press.
- Nevalainen, J., David, L., and Guainazzi, M. (2010). Cross-calibrating X-ray detectors with clusters of galaxies: An IACHEC study. Astronomy & Astrophysics, 523:A22.
- Plucinsky, P. P., Beardmore, A. P., Foster, A., Haberl, F., Miller, E. D., Pollock, A. M., and Sembay, S. (2017). SNR 1E 0102.2-7219 as an X-ray calibration standard in the 0.5-1.0 keV bandpass and its application to the CCD instruments aboard Chandra, Suzaku, Swift and XMM-Newton. Astronomy & Astrophysics, 597(A35).
- Read, A. M., Guainazzi, M., and Sembay, S. (2014). Cross-calibration of the XMM-Newton EPIC pn and MOS on-axis effective areas using 2XMM sources. Astronomy & Astrophysics, 564:A75.

- Rubin, D. B. (1978). Bayesian inference for causal effects: The role of randomization. The Annals of Statistics, 6(1):34–58.
- Schellenberger, G., Reiprich, T., Lovisari, L., Nevalainen, J., and David, L. (2015). XMM-Newton and Chandra cross-calibration using HIFLUGCS galaxy clusters-systematic temperature differences and cosmological impact. Astronomy & Astrophysics, 575:A30.
- Schwartz, D. A. (2014). Invited review article: The Chandra X-ray observatory. Review of Scientific Instruments, 85(6):061101.
- Sembay, S., Guainazzi, M., Plucinsky, P., and Nevalainen, J. (2010). Defining high-energy calibration standards: IACHEC (International Astronomical Consortium for High-Energy Calibration). In AIP Conf. Proceedings, volume 1248, pages 593–594. AIP.
- Seward, F. (1992). Calibration sources for spectral analysis.
- Stan Development Team (2015). Stan Modeling Language User’s Guide and Reference Manual, Version 2.10.0.
- Stan Development Team (2016). Pystan: the Python interface to Stan.
- Tanner, M. A. and Wong, W. H. (1987). The calculation of posterior distributions by data augmentation. Journal of the American Statistical Association, 82(398):528–540.
- Tsujimoto, M., Guainazzi, M., Plucinsky, P. P., Beardmore, A. P., Ishida, M., Natalucci, L., Posson-Brown, J. L., Read, A. M., Saxton, R. D., and Shaposhnikov, N. V. (2011). Cross-calibration of the X-ray instruments onboard the Chandra, Integral, RXTE, Suzaku, Swift, and XMM-Newton observatories using G21. 5–0.9. Astronomy & Astrophysics, 525:A25.
- Watson, M. G., Schröder, A. C., Fyfe, D., Page, C. G., Lamer, G., Mateos, S., Pye, J., Sakano, M., Rosen, S., Ballet, J., Barcons, X., Barret, D., Boller, T., Brunner, H., Brusa, M., Caccianiga, A., Carrera, F. J., Ceballos, M., Della Ceca, R., Denby, M., Denkinson, G., Dupuy, S., Farrell, S., Frascchetti, F., Freyberg, M. J., Guillout, P., Hambaryan, V., Maccacaro, T., Mathiesen, B., McMahon, R., Michel, L., Motch, C., Osborne, J. P., Page, M., Pakull, M. W., Pietsch, W., Saxton, R., Schwope, A., Severgnini, P., Simpson, M., Sironi, G., Stewart, G., Stewart, I. M., Stobbart, A.-M., Tedds, J., Warwick, R., Webb, N., West, R., Worrall, D., and Yuan, W. (2009). The XMM-Newton serendipitous survey. V. The Second XMM-Newton serendipitous source catalogue. Astronomy and Astrophysics, 493:339–373.
- Weatherhead, E. C., Reinsel, G. C., Tiao, G. C., Meng, X.-L., Choi, D., Cheang, W.-K., Keller, T., DeLuisi, J., Wuebbles, D. J., Kerr, J. B., and Miller, A. (1998). Factors affecting the detection of trends: Statistical considerations and applications to environmental data. Journal of Geophysical Research: Atmospheres, 103(D14):17149–17161.
- Woodbury, M. A. (1950). Inverting modified matrices. Memorandum report, 42(106):336.
- XMM Catalogue public pages (2008). XMM-Newton serendipitous source catalogue: 2XMM. http://xmmssc-www.star.le.ac.uk/Catalogue/xcat_public_2XMM.html.
- Xu, J., Van Dyk, D. A., Kashyap, V. L., Siemiginowska, A., Connors, A., Drake, J., Meng, X.-L., Ratzlaff, P., and Yu, Y. (2014). A fully Bayesian method for jointly fitting instrumental calibration and X-ray spectral models. The Astrophysical Journal, 794(2):97.

Appendices

A Details of Fitting the Log-Normal Hierarchical Model

The following three MCMC algorithms are used for our posterior sampling.

1. **Standard Gibbs Sampler:** iterates the following three sets of conditional distributions, all easily derived from (2.7):

- (a) Conditioning on \mathbf{G} and σ^2 , sample B_i independently for $i = 1, \dots, N$ from

$$\mathcal{N}\left(\frac{b_i/\tau_i^2 + \sum_{j \in J_i} (y_{ij} + 0.5\sigma_i^2 - G_j)/\sigma_i^2}{1/\tau_i^2 + \sum_{j \in J_i} 1/\sigma_i^2}, \frac{1}{1/\tau_i^2 + \sum_{j \in J_i} 1/\sigma_i^2}\right).$$

- (b) Conditioning on \mathbf{B} and σ^2 , sample G_j independently for $1 \leq j \leq M$ from

$$\mathcal{N}\left(\frac{\sum_{i \in I_j} (y_{ij} + 0.5\sigma_i^2 - B_i)/\sigma_i^2}{\sum_{i \in I_j} 1/\sigma_i^2}, \frac{1}{\sum_{i \in I_j} 1/\sigma_i^2}\right).$$

- (c) Conditioning on \mathbf{B} and \mathbf{G} , sample σ_i^2 independently for $i = 1, \dots, N$ from

$$\sigma_i^{-|J_i|-2-2\alpha} \exp\left\{-\frac{1}{2} \frac{\sum_{j \in J_i} (y_{ij} - B_i - G_j)^2 + 2\beta}{\sigma_i^2} - \frac{|J_i|\sigma_i^2}{8}\right\}$$

via the Metropolis-Hastings algorithm using a simple random walk proposal (Gaussian proposal) on the log-scale, i.e., $\log(\sigma_i^2)$.

2. **Block Gibbs Sampler:** same as above except replace the two conditional steps (1a) and (1b) by a joint draw of (\mathbf{B}, \mathbf{G}) from $(N+M)$ -dimensional Gaussian with mean $\mathbf{\Omega}(\sigma^2)^{-1}\boldsymbol{\gamma}(\sigma^2)$ and covariance matrix $\mathbf{\Omega}(\sigma^2)^{-1}$; see (2.9) and (2.10) in Section 2.2.
3. **Hamiltonian Monte Carlo (HMC):** samples the entire vector $\boldsymbol{\theta} = \{B_i, G_j, \sigma_i^2\}$ through the non-U-turn HMC sampler (Hoffman and Gelman, 2014), implemented with the **STAN** package. Here we give a brief description of HMC; see Neal (2011) for more details. Let $\pi(\boldsymbol{\theta})$ denote the (unnormalized) joint posterior $\boldsymbol{\theta}$, as given by (2.7). Define potential energy as $U(\boldsymbol{\theta}) = -\log \pi(\boldsymbol{\theta})$ and kinetic energy as $k(\mathbf{p}) = \mathbf{p}^\top \mathcal{M}^{-1} \mathbf{p}$, where \mathcal{M} is a symmetric positive-definite matrix, thus the total energy is $H(\boldsymbol{\theta}, \mathbf{p}) = U(\boldsymbol{\theta}) + k(\mathbf{p})$. We can obtain

samples of $\pi(\boldsymbol{\theta})$ by sampling from the target density $\exp[-H(\boldsymbol{\theta}, \mathbf{p})] \propto \pi(\boldsymbol{\theta}) \exp(-\mathbf{p}^\top \mathcal{M}^{-1} \mathbf{p})$, which is essentially a data-augmentation technique (Tanner and Wong, 1987). By defining the potential energy and kinetic energy, we can propose MCMC moves according to the Hamiltonian dynamics, which explores the parameter space more efficiently by taking bigger and less correlated moves, as opposed to random walk Metropolis-Hastings or a Gibbs sampler. In practice, we use the leapfrog move to approximate the Hamiltonian dynamics. Due to the energy-preserving property of Hamiltonian dynamics, the acceptance rate of the resulting HMC is approximately 1. It is not exactly 1 because we use the (discretized) leapfrog moves to approximate (continuous) Hamiltonian dynamics. The tuning parameters of the HMC algorithm include the covariance matrix \mathcal{M} , the leapfrog step size ϵ , and the number of leapfrog steps L . These are all self-tuned in the **STAN** package.

We compare the performance of these three algorithms using auto-correlation plots of the posterior samples and the effective sample size, in both the simulated and real data examples. Not surprisingly, the Gibbs sampler converges very slowly relative to the other two algorithms. We are able to cross check our results by comparing the samples obtained with the block Gibbs sampler and HMC – they give practically the same posterior distributions.

B Proprieties of the Posterior Distribution

B.1 Propriety of Posterior

Theorem 1. *Under the prior specifications for $\{B_i, G_j, \sigma_i^2 : 1 \leq i \leq N, 1 \leq j \leq M\}$ given in (2.6), the posterior is proper if each source is measured by at least one instrument, i.e., $|I_j| \geq 1$ for all $1 \leq j \leq M$.*

Proof. We prove the propriety of the posterior by first integrating out the G_j first, then the B_i , and finally the σ_i^2 . By (2.7), $p(\mathbf{B}, \mathbf{G}, \boldsymbol{\sigma}^2 | \mathbf{D}, \boldsymbol{\tau}^2)$ is proportional to

$$\prod_{i=1}^N \sigma_i^{-|J_i|-2-2\alpha} \exp \left\{ -\frac{1}{2} \sum_{j=1}^M \sum_{i \in I_j} \sigma_i^{-2} (y'_{ij} - B_i - G_j)^2 - \sum_{i=1}^N \left[\frac{(b_i - B_i)^2}{2\tau_i^2} + \frac{\beta}{\sigma_i^2} \right] \right\}. \quad (\text{B.1})$$

Now for each $1 \leq j \leq M$, if we define a random index \mathcal{I} on I_j such that $\Pr(\mathcal{I} = i) \propto \sigma_i^{-2}$, then

$$\frac{\sum_{i \in I_j} \sigma_i^{-2} (y'_{ij} - B_i - G_j)^2}{\sum_{i \in I_j} \sigma_i^{-2}} = \mathbb{E} [y'_{\mathcal{I}j} - B_{\mathcal{I}} - G_j]^2 \geq [\mathbb{E}(y'_{\mathcal{I}j} - B_{\mathcal{I}}) - G_j]^2. \quad (\text{B.2})$$

Therefore, the first term in the exponential part of (B.1) is less than $-0.5 \left(\sum_{i \in I_j} \sigma_i^{-2} \right) (G_j - C_j)^2$, where $C_j = \mathbb{E}(y'_{\mathcal{I}j} - B_{\mathcal{I}})$ is free of G_j . The property of Normal density (for G_j) then yields

$$\int p(\mathbf{B}, \mathbf{G}, \boldsymbol{\sigma}^2 | \mathbf{D}, \boldsymbol{\tau}^2) d\mathbf{G} \leq C^* \prod_{i=1}^N \sigma_i^{-|J_i|-2-2\alpha} \prod_{j=1}^M \left[\sum_{i \in I_j} \sigma_i^{-2} \right]^{-1/2} \exp \left\{ - \sum_{i=1}^N \left[\frac{(b_i - B_i)^2}{2\tau_i^2} + \frac{\beta}{\sigma_i^2} \right] \right\}$$

where C^* is a constant that depends only on $\mathbf{D}, \boldsymbol{\tau}^2$. Integrating out \mathbf{B} then gives

$$\int \int p(\mathbf{B}, \mathbf{G}, \boldsymbol{\sigma}^2 | \mathbf{D}, \boldsymbol{\tau}^2) d\mathbf{G} d\mathbf{B} \leq C^{**} \prod_{i=1}^N \sigma_i^{-|J_i|-2-2\alpha} \prod_{j=1}^M \left[\sum_{i \in I_j} \sigma_i^{-2} \right]^{-1/2} \exp \left\{ - \sum_{i=1}^N \frac{\beta}{\sigma_i^2} \right\} \quad (\text{B.3})$$

where C^{**} is a constant that depends only on $\mathbf{D}, \boldsymbol{\tau}^2$. Since I_j is non-empty, it is meaningful to invoke the well-known harmonic-geometric mean inequality to obtain that

$$\prod_{j=1}^M \left[\sum_{i \in I_j} \sigma_i^{-2} \right]^{-1/2} \leq \prod_{j=1}^M |I_j|^{-1/2} \left[\prod_{i \in I_j} \sigma_i \right]^{1/|I_j|} \leq \prod_{i=1}^N \sigma_i^{\sum_{j \in J_i} |I_j|^{-1}}. \quad (\text{B.4})$$

Inequalities (B.3) and (B.4) together imply that the unnormalized $p(\boldsymbol{\sigma}^2 | \mathbf{D}, \boldsymbol{\tau}^2)$ is dominated above by a constant times $\prod_{i=1}^N p_i(\sigma_i^2)$, where $p_i(x)$ is the density of the inverse Gamma distribution with shape parameter $\alpha_i = \alpha + [|J_i| - \sum_{j \in J_i} |I_j|^{-1}]/2$ and scale parameter β . Because $|I_j| \geq 1$, we have $\alpha_i \geq \alpha$. Hence as long as the hyperparameter $\alpha > 0$, which is always chosen to be so, p_i is a proper density. Consequently, $p(\boldsymbol{\sigma}^2 | \mathbf{D}, \boldsymbol{\tau}^2)$ is a proper density after renormalization. □

B.2 Identifiability

When τ_i^2 is large, the likelihood information for estimating B_i (i.e., from c_{ij}) dominates the prior information (i.e., from b_i). In the extreme case of $\tau_i^2 = \infty$, the model is not identifiable because for fixed variances, $\{B_i, G_j\}$ and $\{B_i + \delta, G_j - \delta\}$ yield the same posterior densities for (\mathbf{B}, \mathbf{G}) for any

constant δ . Let λ_{\max} and λ_{\min} be the maximum and minimum eigenvalues of $\mathbf{\Omega}(\boldsymbol{\sigma}^2)$, as defined in Section 2.2. Taking $u = (\mathbf{1}_N, \mathbf{1}_M)^\top$ and $v = (\mathbf{1}_N, -\mathbf{1}_M)^\top$, the *condition number* of $\mathbf{\Omega}(\boldsymbol{\sigma}^2)$ is

$$\frac{\lambda_{\max}}{\lambda_{\min}} \geq \frac{u^\top \mathbf{\Omega}(\boldsymbol{\sigma}^2) u}{v^\top \mathbf{\Omega}(\boldsymbol{\sigma}^2) v} = 1 + \frac{4 \sum_{i=1}^N |J_i| \sigma_i^{-2}}{\sum_{i=1}^N \tau_i^{-2}}, \quad (\text{B.5})$$

where $\mathbf{1}_n$ denotes an $n \times 1$ vector of ones. As a consequence, when $\{\tau_i^2\}$ are generally larger than $\{\sigma_i^2\}$, the ratio in (B.5) can be large, and the posterior contours, determined by $\mathbf{\Omega}$, are elongated in one direction and narrow in another. This provides a guideline that $\{\tau_i^2\}$ should not be set too large relative to $\{\sigma_i^2\}$ in practice, because large $\{\tau_i^2\}$ can lead to near model non-identifiability and consequently more costly computation. A computationally cheaper way of dealing with possible model non-identifiability is to set one of the $\{B_i\}$ equal to a fixed value, which is equivalent to setting the corresponding $\tau_i = 0$. We experiment with this computationally cheap strategy in our empirical evaluations, and find that it does not alter the results in substantive ways, but the resulting estimators for the Effective Areas are relative to some (arbitrarily) chosen values instead of in absolute terms/magnitudes.

C Derivation of Conditional Covariance Matrix

In this section, we give detailed derivations of $\mathbf{\Omega}^{-1}(\boldsymbol{\sigma}^2)$ when all instruments measure all sources. In this case, W_i defined in (2.13) becomes $W_i = \frac{M\sigma_i^{-2}}{M\sigma_i^{-2} + \tau_i^{-2}}$, $1 \leq i \leq N$. Define $\tilde{\sigma}^2 = \left(N^{-1} \sum_{i=1}^N \sigma_i^{-2}\right)^{-1}$.

Let \mathbf{A} be the $(N + M) \times (N + M)$ diagonal matrix with diagonal elements equal to those of $\mathbf{\Omega}(\boldsymbol{\sigma}^2)$. Let \mathbf{U} be an $(N + M) \times 2$ matrix such that $U_{i,1} = \sigma_i^{-2}$, $U_{i,2} = 0$ for $i = 1, \dots, N$, and $U_{j+N,1} = 0$, $U_{j+N,2} = 1$ for $j = 1, \dots, M$. Let \mathbf{C} be a 2×2 matrix such that $C_{i,j} = I_{i \neq j}$ ($i, j = 1, 2$). Then $\mathbf{\Omega}(\boldsymbol{\sigma}^2) = \mathbf{A} + \mathbf{U}\mathbf{C}\mathbf{U}^\top$. By the Woodbury matrix identity, we have

$$\mathbf{\Omega}^{-1}(\boldsymbol{\sigma}^2) = \mathbf{A}^{-1} - \mathbf{A}^{-1}\mathbf{U} (\mathbf{C} + \mathbf{U}^\top \mathbf{A}^{-1} \mathbf{U})^{-1} \mathbf{U}^\top \mathbf{A}^{-1}, \quad (\text{C.1})$$

where \mathbf{A}^{-1} is a diagonal matrix with diagonal elements

$$\left(\{W_i \sigma_i^2 / M\}_{1 \leq i \leq N}, \{\tilde{\sigma}^2 / N\}_{1 \leq j \leq M} \right).$$

Therefore, we can derive the inverse of 2×2 matrix $\mathbf{C} + \mathbf{U}^\top \mathbf{A}^{-1} \mathbf{U}$ as

$$(\mathbf{C} + \mathbf{U}^\top \mathbf{A}^{-1} \mathbf{U})^{-1} = \begin{pmatrix} \frac{\sum_{i=1}^N W_i \sigma_i^{-2}}{M} & 1 \\ 1 & \frac{M}{N} \tilde{\sigma}^2 \end{pmatrix}^{-1} = -\frac{\sum_{i=1}^N \sigma_i^{-2}}{\sum_{i=1}^N W_i \tau_i^{-2}} \begin{pmatrix} \frac{M^2 \tilde{\sigma}^2}{N} & -M \\ -M & \sum_{i=1}^N W_i \sigma_i^{-2} \end{pmatrix}.$$

Further, let \mathbf{W} be the $N \times 1$ column vector with i th element W_i , then we have

$$\mathbf{A}^{-1} \mathbf{U} = \begin{pmatrix} \mathbf{W}/M & 0_{N \times 1} \\ 0_{M \times 1} & \tilde{\sigma}^2/N \mathbf{1}_{M \times 1} \end{pmatrix}.$$

Consequently, $\mathbf{A}^{-1} \mathbf{U} (\mathbf{C} + \mathbf{U}^\top \mathbf{A}^{-1} \mathbf{U})^{-1} \mathbf{U}^\top \mathbf{A}^{-1}$ is equal to

$$-\left(\sum_{i=1}^N \tau_i^{-2} W_i\right)^{-1} \begin{pmatrix} \mathbf{W} \mathbf{W}^\top & -\mathbf{W} \mathbf{1}_{1 \times M} \\ -\mathbf{1}_{M \times 1} \mathbf{W}^\top & [N^{-1} \tilde{\sigma}^2] \sum_{i=1}^N W_i \sigma_i^{-2} \mathbf{1}_{M \times M} \end{pmatrix}.$$

Finally, we arrive at the closed-form expression for $\boldsymbol{\Omega}^{-1}(\boldsymbol{\sigma}^2)$:

$$\begin{aligned} (\boldsymbol{\Omega}^{-1}(\boldsymbol{\sigma}^2))_{i,i} &= \frac{1}{M \sigma_i^{-2} + \tau_i^{-2}} \left\{ 1 + \frac{M \sigma_i^{-2} W_i}{\sum_{u=1}^N \tau_u^{-2} W_u} \right\}, \\ (\boldsymbol{\Omega}^{-1}(\boldsymbol{\sigma}^2))_{i,j+N} &= (\boldsymbol{\Omega}^{-1}(\boldsymbol{\sigma}^2))_{j+N,i} = -W_i \left(\sum_{u=1}^N \tau_u^{-2} W_u \right)^{-1}, \\ (\boldsymbol{\Omega}^{-1}(\boldsymbol{\sigma}^2))_{j+N,j+N} &= \left(\sum_{u=1}^N \sigma_u^{-2} \right)^{-1} \left\{ 1 + \frac{\sum_{i=1}^N W_i \sigma_i^{-2}}{\sum_{u=1}^N W_u \tau_u^{-2}} \right\}. \end{aligned}$$

D Likelihood Method

D.1 MLEs and Their Asymptotic Variances

Note that the variance-covariance matrix of the MLEs $(\hat{\mathbf{B}}, \hat{\mathbf{G}})$ is in fact $\boldsymbol{\Omega}^{-1}(\boldsymbol{\sigma}^2)$ as defined in (2.10). Therefore, we have the following proposition.

Proposition 1. *If all detectors measure all objects, i.e., $J_i = \{1, \dots, M\}$, $I_j = \{1, \dots, N\}$ and $\{\sigma_i^2, \tau_i^2\}$ are known constants, then the variances of $\{\hat{B}_i\}$, $\{\hat{G}_j\}$ are given by*

$$\text{Var}(\hat{G}_j) = \left[\sum_{i=1}^N \sigma_i^{-2} \right]^{-1} \mathcal{S}_G, \quad \text{Var}(\hat{B}_i) = [M \sigma_i^{-2} + \tau_i^{-2}]^{-1} \mathcal{S}_B^{(i)}, \quad (\text{D.1})$$

where the inflation factors $\mathcal{S}_G, \{\mathcal{S}_B^{(i)}\}$ are given by

$$\mathcal{S}_G = 1 + \frac{\sum_{i=1}^N \sigma_i^{-2} W_i}{\sum_{i=1}^N \tau_i^{-2} W_i}, \quad \mathcal{S}_B^{(i)} = 1 + \frac{M \sigma_i^{-2} W_i}{\sum_{u=1}^N \tau_u^{-2} W_u}.$$

Moreover, we have $\text{Cov}(\hat{B}_i, \hat{G}_j) = -W_i \left[\sum_{k=1}^N \tau_k^{-2} W_k \right]^{-1}$.

Remark 1. Under the additive model, B_i and G_j are negatively correlated for all i, j . The asymptotic variances of \hat{B}_i and \hat{G}_j can be written as

$$\text{Var}(\hat{G}_j) = \text{Var}(\tilde{G}_j) \mathcal{S}_G, \quad \text{Var}(\hat{B}_i) = \text{Var}(\tilde{B}_i) \mathcal{S}_B^{(i)},$$

where $\text{Var}(\tilde{G}_j) = \left[\sum_{i=1}^N \sigma_i^{-2} \right]^{-1}$ is the inverse precision, i.e., asymptotic covariance, of \hat{G}_j when the B_i are known constants; $\text{Var}(\tilde{B}_i) = [M \sigma_i^{-2} + \tau_i^{-2}]^{-1}$ is the inverse precision, i.e., asymptotic covariance, of \hat{B}_i when the G_j are known constants. The inflation factors \mathcal{S}_G and $\mathcal{S}_B^{(i)}$ adjust for the fact that none of the B_i or the G_j are known.

Proposition 1 directly yields the following asymptotic results as $N, M \rightarrow \infty$.

Corollary 1. If $\{\sigma_i/\tau_i\}$ are uniformly bounded from below and above by finite positive constants, and $\sum_{i=1}^N \sigma_i^{-2}/N$ converges to a positive constant as $N \rightarrow \infty$, then for all i, j , as $N, M \rightarrow \infty$,

$$\text{Var}(\hat{G}_j) = O(N^{-1}), \quad \text{Var}(\hat{B}_i) = O(N^{-1} + M^{-1}), \quad \text{Cov}(\hat{B}_i, \hat{G}_j) = -O(N^{-1}).$$

Specifically, when $\tau = \tau_1 = \dots = \tau_N$ and $\sigma = \sigma_1 = \dots = \sigma_N$, (D.1) simplifies to

$$\text{Var}(\hat{G}_j) = \frac{\sigma^2}{N}, \quad \text{Var}(\hat{B}_i) = \frac{1}{M \sigma^{-2} + \tau^{-2}} \left(1 + \frac{M \sigma^{-2}}{N \tau^{-2}} \right), \quad \text{Cov}(\hat{B}_i, \hat{G}_j) = -\frac{\tau^2}{N}.$$

Remark 2. The results above show that the asymptotic variances for $\{B_i\}$ and $\{G_j\}$ are not ‘exchangeable’ (i.e., switching \mathbf{B} and \mathbf{G} and correspondingly N and M), mainly for three reasons: first, for each B_i we assign an informative prior $\mathcal{N}(b_i, \tau_i^2)$ whereas for each G_j we assign a flat prior on the real line; second, for each instrument i , besides B_i , we also need to estimate σ_i^2 ; last, the measurement uncertainty depends only on the instrument but not on the sources (recall that $\sigma_{ij}^2 = \sigma_i^2$ for all i, j).

D.2 Goodness-of-fit

We now give a goodness-of-fit test statistic for the random-effect regression model. Under the model (2.6), we have the following normalized residual sum of squares:

$$T(\mathbf{B}, \mathbf{G}) := \sum_{i=1}^N \frac{(b_i - B_i)^2}{\tau_i^2} + \sum_{i=1}^N \sum_{j=1}^M \frac{(y'_{ij} - B_i - G_j)^2}{\sigma_i^2}. \quad (\text{D.2})$$

We see this sum of squares has two parts. The first part involves $\{b_i\}$ only, measuring how good the prior means are relative to the prior variances $\{\tau_i\}$. The second part depends on $\{y_{ij}\}$ only, and it will allow us to assess how good the fitted \mathbf{B}, \mathbf{G} are relative to the sampling variances σ^2 . Here we put them together as an overall model check, but one can certainly use them individually if one wants to check the prior distribution and likelihood model separately.

Theorem 2. *When the variances σ_i^2, τ_i^2 are known and we insert the MLEs of B_i and G_j into (D.2), we obtain $T(\hat{\mathbf{B}}, \hat{\mathbf{G}}) \sim \chi_{NM-M}^2$.*

Proof. This conclusion regarding χ^2 distribution follows from standard results on residual sum of squares of linear regression with Gaussian error. To figure out the correct degrees of freedom, we have $(NM + N)$ independent observations in total, but with $N + M$ parameters. Therefore, the degrees of freedom for the residual sum of squares is $NM - M$. \square

With unknown variances we do not have a closed-form distribution of T as defined in formula (D.2). Heuristically, we invoke the standard large-sample arguments and to continuously use the χ^2 approximation, but reduce the degrees of freedom to $MN - M - N$ to count for the number of estimated variance parameter $\{\sigma_i^2\}$. The resulting p-values of the fitted data in Sections 4.2 and 4.3 are not significant.

E More Simulation Results Under Misspecified Models

In Simulations IV and V, we generate data as $c_{ij} = \lambda_{ij}X_{ij}$, where $X_{ij} \sim \text{Poisson}(A_i F_j)$, and independently $\lambda_{ij} \sim \text{Uniform}[0.8, 1.2]$ for Simulation IV and $\lambda_{ij} \sim \text{Uniform}[0.4, 1.6]$ for Simulation V. In Simulations VI and VII, we generate data from $c_{ij} \sim \text{Poisson}(\lambda_{ij}A_i F_j)$, where the λ_{ij} are randomly generated from the uniform distribution on $[0.8, 1.2]$. The other parameters are set to be

the same as in Simulation II except that $\beta = 0.01$ for these simulations. Simulations VI and VII resemble the cases where the true model is Poisson and the estimation of T_{ij} is volatile, whereas Simulations IV and V resemble the cases that happen in practice, where the photon counts are multiplied by an adjustment factor, such as \hat{T}_{ij}^{-1} , as with the data pre-processing step for the XCAL data.

Figure 10 gives the results of Simulations IV and V. Figure 11 gives the results of Simulation VI with smaller counts ($B_i = 1$ and $G_j = 3$) and VII with larger counts ($B_i = 5$ and $G_j = 3$) under this scenario. It shows with large Poisson counts, controlling the uncertainty in the multiplicative constant can possibly lead to reasonably good results. Thus, even with compounded model misspecification, the log-Normal hierarchical model is able to provide reasonable, though not as precise, results, as compared with the correctly-specified case. However, when the misspecified “known constant” is highly variable, the fit result is not as satisfactory; plugging in a “guesstimated” σ_i in this case can give disastrously optimistic but biased results.

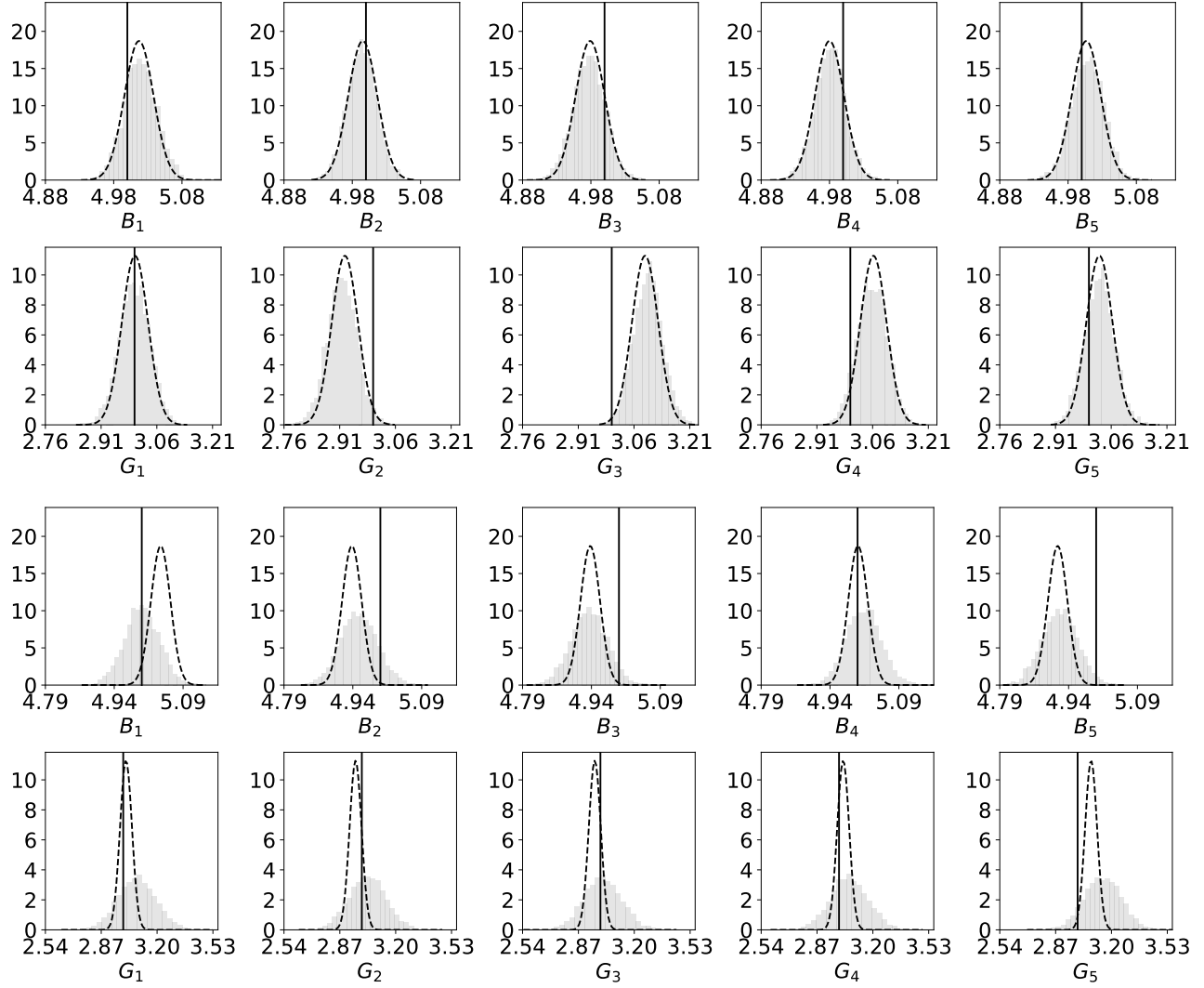


Figure 10: Simulations IV (rows 1 & 2) and V (rows 3 & 4). The gray shades are the posterior distributions of $\{B_i\}_{i=1}^5$ (rows 1 & 3) and $\{G_j\}_{j=1}^5$ (rows 2 & 4) fitted with unknown variances. The solid vertical black lines denote the true values. The black dashed density curves on top of the histograms denote the true posterior densities of $\{B_i\}$ and the $\{G_j\}$ with ‘known’ variances $\sigma_i^2 = 0.1^2$.

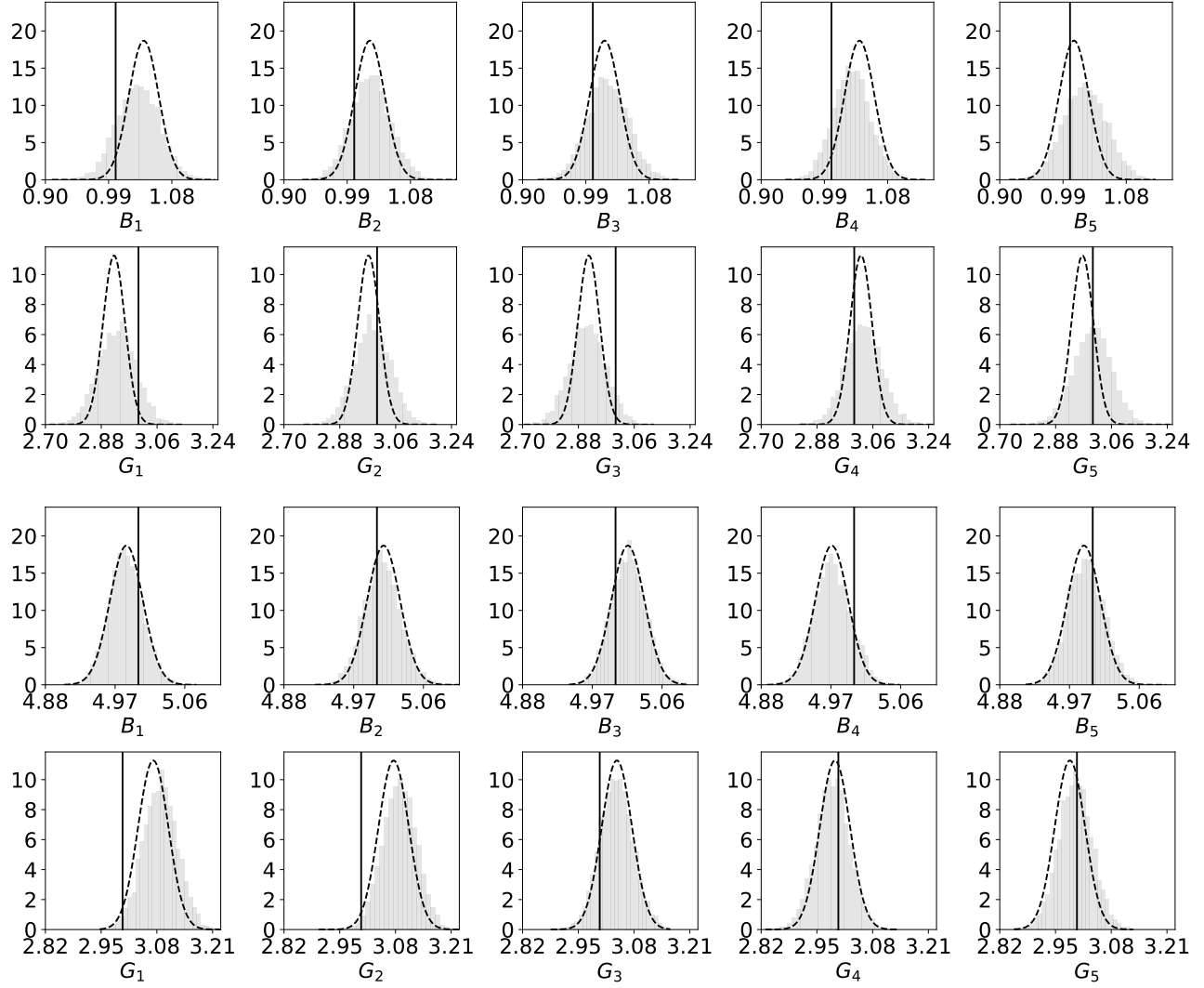


Figure 11: Same as Figure 10 but with Simulations VI (rows 1 & 2) and VII (rows 3 & 4).